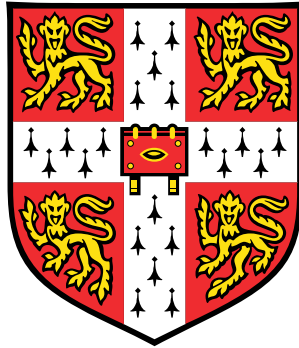


Simulating a Few Interacting Particles in a Flat Band

Part III Project Report



Candidate Number: 8242T

Supervisor: Prof. U.W. Schneider

Department of Physics

University of Cambridge

13th May, 2024

Word Count: 4922

Except where specific reference is made to the work of others, this work is original and has not been already submitted either wholly or in part to satisfy any degree requirement at this or any other university.

Lab Book: https://1drv.ms/u/s!AgEsvYduOSl0mEK8AZsgs_dfKQh8

Abstract

The non-equilibrium time-dynamics of one and two bosons in a kagome lattice are investigated through exact numerical simulations with the Bose-Hubbard Hamiltonian. The kagome bandstructure contains a dispersionless ‘flat band’; single particles in the flat band are observed to remain stationary indefinitely. Interactions between particles are found to lift the degeneracy of the flat band, enabling transport of bound particle pairs in the weak-interaction limit; for strong interactions, the particles are independently mobile. The strong-interaction eigenspectrum divides into a ‘scattering’ band and a ‘doublon’ band, whose respective dynamical behaviours are analysed. This research provides a detailed microscopic account of the one- and two-boson physics in the kagome lattice across the full range of interaction strengths.

Contents

Abstract	ii
1 Introduction	1
2 Theoretical Background and Literature	3
2.1 Bose-Hubbard Model	3
2.2 Kagome Lattice and Bandstructure	4
2.3 Interactions in Flat Bands	6
2.4 Strong-Interaction Regime	7
2.5 Summary and Project Aims	8
3 Methodology	10
3.1 Computational Implementation	10
3.2 Evaluating Time-Evolution	10
4 Single-Particle Simulations	12
4.1 Single-Site Initial State	12
4.2 Stationary Density	12
5 Two-Particle Simulations	15
5.1 Flat Band Initial State	15
5.1.1 Dynamical Behaviour and Interaction-Shifted Eigenspectrum	17
5.1.2 Dependence on Interaction Strength	18

5.1.3	OPDM and Flat Band Projection	20
5.2	Strong Interactions	22
5.2.1	Eigenspectrum	22
5.2.2	Dynamical Behaviour	22
5.3	Particle Separation	23
5.3.1	Expected Separation	24
5.3.2	Radial Distribution Function	25
6	Conclusions	28
A	Pair Energy in Isolated Flat Band Limit	30
B	Further Computational Details	33
B.1	Comparison of Numerical Routines	33
B.2	Three-Particle Computation Time	35
C	Single-Site Initial State with Interactions	36
D	Further Strong-Interaction Results	38
D.1	Higher-Order Corrections to Doublon Energies	38
D.2	Doublon Fraction	39
	Bibliography	41

1. Introduction

In dispersionless (‘flat’) Bloch bands, the energy is constant and independent of momentum [1]. The physics of systems with flat bands is therefore dominated by interactions rather than the kinetic energy, leading to various interesting strongly-correlated phenomena. Notable recent topics of research include fractional and anomalous quantum Hall physics [2–7], topological states of matter [8–13], unconventional superconductivity [14–19], and other exotic phases [20–22].

Flat bands arise in tight-binding models on certain lattices, including the dice lattice [23], Lieb lattice [24], and the kagome lattice [25], the subject of this project. Previous research has predominantly studied the rich equilibrium behaviour of kagome systems (which originates from the Dirac cones in the bandstructure and the frustrated geometry, as well as the flat band). Numerical studies have predicted numerous topological phases [10, 26–28], exotic superfluid phases [20, 21, 29–31], and distinctive magnetic properties, including ‘spin liquids’ [32–35]. Simultaneously, experimental research has observed topological flat bands [12, 13], unconventional superconductivity [11, 18, 19] and the anomalous Hall effect [6, 7] in kagome materials. There is, however, little research into non-equilibrium, dynamical behaviour in kagome systems, which this project will address. This limited relevant prior research will be detailed in Section 2.

Beyond this scarcity of existing research, another motivation for this project is the emerging capability of experimentally studying dynamics in kagome systems, through quantum simulation with ultracold atoms [36, 37]. This experimental field involves creating an optical lattice with lasers, forming an effective potential landscape for (fermionic or bosonic) alkali atoms. These experiments have numerous advantages over traditional condensed matter sys-

tems: they are well-described by simple Hamiltonians with controllable parameters; they are defect-free; the absence of dissipation and decoherence mechanisms facilitate investigating non-equilibrium physics [38]; and the dynamical timescales are sufficiently long to be resolved [39].

Although the kagome lattice was first realised in such an experiment in 2012 [40], the flat band is the highest in energy in the kagome bandstructure and therefore difficult to populate. Consequently, previous cold atom flat band research has mainly employed the Lieb lattice [1]. However, techniques for preparing negative-temperature cold atom systems have been demonstrated [41]. Here, the higher-energy states are more populated, opening the possibility of flat band research using optical kagome lattices. This project complements the ongoing experimental research in this field by my supervisor, Prof. Ulrich Schneider.

In this report, exact numerical simulations of bosonic kagome systems are presented, with a particular focus on the effects of interactions within the flat band. A fundamental, microscopic understanding of the behaviour of one- and two-particle systems is developed for different regimes of interaction strength. Computational limitations precluded studying systems with greater particle numbers, as discussed in Appendix B.2. The report is structured as follows. Section 2 sets out the relevant theoretical background and literature, following which the scope and aims of the project can be described in more detail. Section 3 details the methodology of the computational simulations. Section 4 presents single-particle simulations, and Section 5 two-particle simulations, with the dynamical behaviour examined both qualitatively and quantitatively. Finally, Section 6 gives the conclusions and outlook from the project.

2. Theoretical Background and Literature

2.1 Bose-Hubbard Model

The Hamiltonian investigated throughout this project is the Bose-Hubbard (BH) model:

$$H = H_J + H_U \tag{2.1a}$$

$$H_J = -J \sum_{\langle ij \rangle} b_i^\dagger b_j + \text{H.c.} \tag{2.1b}$$

$$H_U = \frac{U}{2} \sum_i n_i(n_i - 1) \tag{2.1c}$$

Hats are omitted from operators. b_i^\dagger and b_i are bosonic creation and annihilation operators, and $n_i = b_i^\dagger b_i$ the number operator, at site i . H_J represents hopping between all nearest-neighbour sites $\langle ij \rangle$ with amplitude $J \geq 0$. H_U is the on-site repulsive interaction energy between particles with strength $U \geq 0$. The ratio U/J determines the behaviour regime; J was set to 1 throughout the project. The BH model neglects hoppings to beyond-nearest-neighbour sites, interactions between particles on different sites, and assumes contact interactions (s -wave scattering). These approximations are all appropriate for cold atoms in a sufficiently deep optical potential [42].

2.2 Kagome Lattice and Bandstructure

The kagome lattice (Fig. 2.1(a)) is a hexagonal Bravais lattice, with a triangular three-site basis in each unit cell. The lattice vectors are $\mathbf{a}_1 = a(1, 0)$ and $\mathbf{a}_2 = a(1/2, \sqrt{3}/2)$, with a the lattice constant.

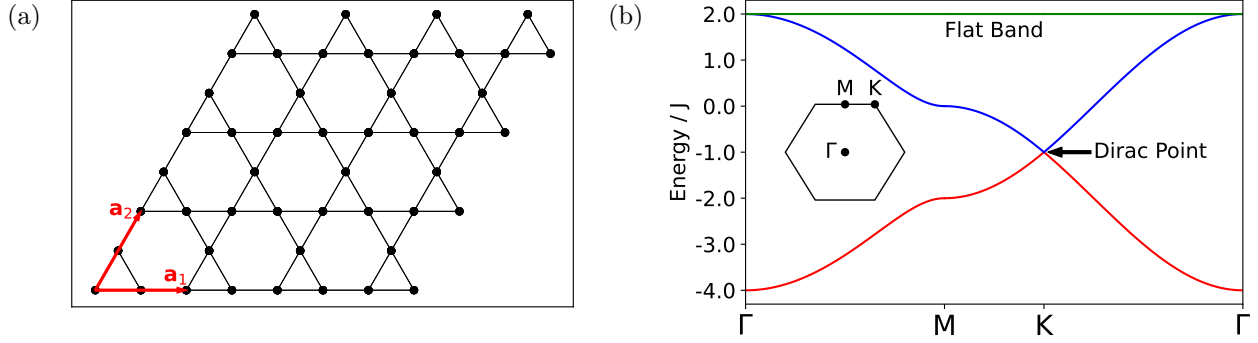


Figure 2.1: (a) Kagome lattice section, with lattice vectors in red. (b) Single-particle bandstructure, with the first Brillouin zone inset. The highest-energy band (green) is flat.

The single-particle bandstructure of the Kagome lattice (Fig. 2.1(b)) is obtained through a Fourier transform:

$$b_{\mathbf{k}\alpha} = \frac{1}{\sqrt{N_c}} \sum_i e^{-i\mathbf{k}\cdot\mathbf{r}_{i\alpha}} b_{i\alpha} \quad (2.2)$$

where the sum runs over unit cells i (not individual sites as in Eq. 2.1), the number of unit cells is N_c , and α indexes the three sites in the unit cell. The Hamiltonian becomes:

$$H_J = \sum_{\mathbf{k}, \alpha, \beta} b_{\mathbf{k}\alpha}^\dagger \mathcal{H}_{\alpha\beta}(\mathbf{k}) b_{\mathbf{k}\beta} \quad (2.3a)$$

$$\mathcal{H}(\mathbf{k}) = -2J \begin{pmatrix} 0 & \cos k_3 & \cos k_2 \\ \cos k_3 & 0 & \cos k_1 \\ \cos k_2 & \cos k_2 & 0 \end{pmatrix} \quad (2.3b)$$

where \mathbf{k} is in the first Brillouin zone, $k_i = \mathbf{k} \cdot \mathbf{a}_i / 2$ for $i = 1, 2$, and $k_3 = k_2 - k_1$. Diagonalizing $\mathcal{H}(\mathbf{k})$ gives the three energy bands:

$$E_{\mathbf{k}}^{(1,2)} = J(-1 \pm \sqrt{4(\cos^2 k_1 + \cos^2 k_2 + \cos^2 k_3) - 3}) \quad (2.4a)$$

$$E_{\mathbf{k}}^{(3)} = 2J \quad (2.4b)$$

The flat band eigenvector is:

$$\mathbf{m}_{\mathbf{k}}^{(3)} = \frac{1}{\sqrt{\sin^2 k_1 + \sin^2 k_2 + \sin^2 k_3}} \begin{pmatrix} \sin k_3 \\ -\sin k_2 \\ \sin k_1 \end{pmatrix} \quad (2.5)$$

The dispersive band eigenvectors are not required in this project. The components of $\mathbf{m}_{\mathbf{k}}^{(3)}$, denoted $m_{\mathbf{k}\alpha}^{(3)}$, define the single-particle flat band Bloch states:

$$|\mathbf{k}\rangle = \sum_{\alpha} m_{\mathbf{k}\alpha}^{(3)} b_{\mathbf{k}\alpha}^{\dagger} |0\rangle \quad (2.6)$$

The group velocity of particles is:

$$\mathbf{v}_g = \frac{1}{\hbar} \nabla_{\mathbf{k}} E_{\mathbf{k}} \quad (2.7)$$

Particles in the flat band are therefore stationary, with $\mathbf{v}_g = 0$. In the real-space picture, the extensive degeneracy of the flat band states enables the construction of spatially localised eigenstates. The most localised possible state is hexagonal (see Fig. 2.2); the localisation can be intuitively understood as arising from destructive interference preventing hopping outside the hexagon. Non-overlapping hexagons form many-particle flat band eigenstates; however, the hexagons are not orthonormal, and cannot be used as a basis for the flat band [29].

For Hubbard systems with a single fermionic species, the behaviour is effectively non-interacting since the Pauli principle forbids multiple occupancy of any site. Past numerical simulations of such systems have confirmed that particles in dispersive bands are mobile, whereas particles in flat bands remain stationary indefinitely [43–45].

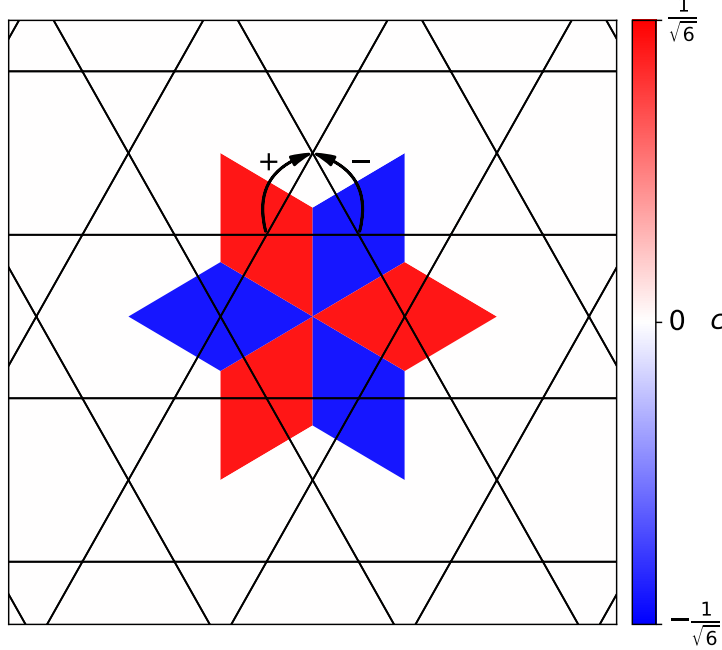


Figure 2.2: Hexagonal flat band eigenstate. The amplitude of $|\Psi\rangle$ at each site, $c_i = \langle 0|b_i|\Psi\rangle$, is shown. Destructive interference between sites with opposite signs prevents hopping outside the hexagon, as illustrated. In this plot and others throughout the report, to eliminate blank space, the entire area closest to a given lattice site is coloured according to the value of the quantity being plotted (here, c_i) at that site.

2.3 Interactions in Flat Bands

For weak interactions, $U \ll J$, H_U can be treated as a perturbation to H_J . Direct products of single-particle eigenstates are therefore good two-particle eigenstates, but with their eigenvalues shifted (in general) by the interaction energy. This partially lifts the degeneracy in the flat band, enabling particle mobility. However, for two single-particle flat band states with no real-space overlap, there is no interaction energy shift to the eigenvalues; the particles therefore remain stationary. Accordingly, particles are only expected to propagate in bound pairs.

In [46], expressions for the energy eigenvalues of bound particle pairs are derived in terms

of the Bloch eigenvectors (Eq. 2.5), for systems with an isolated flat band (not strictly accurate for the kagome lattice, whose second band touches the flat band, see Fig. 2.1(b)). The energy shifts relative to the flat band are determined by the total momentum of the particles, $\mathbf{q} = \mathbf{k}_1 + \mathbf{k}_2$, and are proportional to U :

$$\Delta E_{\mathbf{q}} \propto U \quad (2.8)$$

See Appendix A for further mathematical details; the errors due to the isolated flat band approximation turn out to be minor. Although this theoretical framework exists, however, the interaction-shifted eigenspectrum, and the resulting dynamical behaviour, are yet to be determined for the kagome lattice.

The dynamical effects of interactions lifting the degeneracy in (non-kagome) flat band systems are investigated numerically in [44, 45]. Instead of remaining localized in flat band states like (effectively non-interacting) spinless fermions, bosons propagate from their initial state. These papers only cover the limiting case of $U \rightarrow \infty$. The qualitative interpretation that interactions break the flat band degeneracy, enabling transport, is the same as the weak-interaction case described above; however, neither the dependence of the behaviour on (finite) interaction strength, nor the kagome lattice specifically, are considered.

Cold atom experiments investigating Lieb [47] and kagome [48] systems have similarly found that interacting bosons in (formerly) flat bands acquire non-zero group velocities. This is explained as the interaction energy renormalizing the lattice potential energy within the Gross-Pitaevskii equation. In contrast to these many-particle, mean-field methods, this project adopts a few-particle, microscopic approach. Although the effect of interactions may be qualitatively similar in enabling transport, the details of the behaviour for the systems considered here are unknown.

2.4 Strong-Interaction Regime

In the strong-interaction limit, $U \gg J$, the interaction energy far exceeds the maximum possible kinetic energy. With no dissipation mechanisms (as in cold atom experiments), particles on the same site cannot separate while conserving energy, and are therefore ‘repulsively

bound' together as a 'doublon'. Similarly, particles on separate sites cannot subsequently occupy the same site. The eigenspectrum of the system therefore splits into a high-energy doublon band, and a low-energy 'scattering' band, with eigenstates composed of doubly- and singly- occupied sites respectively [49, 50]. Cold atom experiments, firstly [51], have verified this theoretical prediction.

The doublon band can be modelled by an effective single-particle Hamiltonian with an energy offset E_0 and hopping coefficient J_{eff} . Using second-order perturbation theory, these are given by [52]:

$$H_{\text{eff}} = E_0 - J_{\text{eff}} \sum_{\langle ij \rangle} d_i^\dagger d_j + \text{H.c.} \quad (2.9a)$$

$$E_0 = \langle d_i | H | d_i \rangle + \sum_s \frac{|\langle s | H | d_i \rangle|^2}{E_d - E_s} = U + \frac{8J^2}{U} \quad (2.9b)$$

$$J_{\text{eff}} = - \sum_s \frac{\langle d_j | H | s \rangle \langle s | H | d_i \rangle}{E_d - E_s} = -\frac{2J^2}{U} \quad (2.9c)$$

Here, $d_i^\dagger = \frac{1}{\sqrt{2}}(b_i^\dagger)^2$ creates a doublon on site i , $|d_i\rangle = d_i^\dagger|0\rangle$, $|s\rangle$ is a virtual intermediate (scattering) state, and H is the BH Hamiltonian (Eq. 2.1). The hopping amplitude has the opposite sign to Eq. 2.1.

2.5 Summary and Project Aims

This section has presented the existing theory and research relating to dynamics in flat band systems, and the kagome lattice specifically. Without interactions, particles in flat band states are immobile; interactions lift the degeneracy of the flat band, enabling transport. Previous numerical and experimental research is all consistent with this general behaviour. Additionally, for strong interactions, a separation of doublon and scattering states is expected.

However, there is a lack of research into the specific subject of this project: the non-equilibrium dynamics of small numbers of bosons in a kagome lattice. Previous research has concerned either fermions [43], different lattices [44–47], or mean-field cases [47, 48]; the details of the physics in the systems considered here are unknown. Moreover, the full range of interaction strengths has not been investigated.

In this report, different behaviour regimes are systematically investigated, developing a broad understanding of one- and two-boson kagome systems. Single-particle simulations are discussed in Section 4, and quantitatively tested against the theoretical predictions from the single-particle bandstructure. Two-particle results are presented in Section 5. The relationship between interaction strength and particle mobility is investigated and explained for states which, without interactions, would be stationary, localised flat band states. For strong interactions, the eigenspectrum of the system is compared to the theoretical predictions of Section 2.4, and the resulting dynamical behaviour examined.

3. Methodology

3.1 Computational Implementation

The simulations were performed using Python, on a Macbook Air with a 1.1 GHz Quad-Core Intel Core i5 processor and 8GB RAM. The Hamiltonian (Eq. 2.1) was expressed as a matrix in a basis of Fock states of the system. For one particle, these basis states are $b_i^\dagger|0\rangle$ for all sites i ; and for two particles, $b_i^\dagger b_j^\dagger|0\rangle$ for all pairs of (different) sites ij , and $\frac{1}{\sqrt{2}}(b_i^\dagger)^2|0\rangle$ when both particles occupy site i . The state of the system is represented by a vector \mathbf{c} of the coefficients c_α of the basis states $|\alpha\rangle$ in the expansion of $|\Psi\rangle$:

$$|\Psi\rangle = \sum_{\alpha} c_{\alpha} |\alpha\rangle \quad (3.1a)$$

$$c_{\alpha} = \langle \alpha | \Psi \rangle \quad (3.1b)$$

Both periodic (illustrated in Fig. 3.1) and open boundary conditions were implemented. Except where stated otherwise, the results throughout this report are for periodic systems, which are generally less susceptible to finite-size effects.

3.2 Evaluating Time-Evolution

Time-evolution of the quantum state was calculated using one of two methods:

1. The eigenstate method: the Hamiltonian is fully diagonalized to obtain the eigenvalues $\{\epsilon_n\}$ and eigenstates $\{|\phi_n\rangle\}$. $|\Psi(t')\rangle$ is calculated by expanding $|\Psi(t)\rangle$ in terms of $\{|\phi_n\rangle\}$:

$$|\psi(t')\rangle = \sum_n \exp\left(-\frac{i\epsilon_n(t' - t)}{\hbar}\right) \langle \phi_n | \psi(t) \rangle |\phi_n\rangle \quad (3.2)$$

2. The propagator method: the time-evolution is calculated with the exponential of the Hamiltonian:

$$|\psi(t')\rangle = \exp\left(-\frac{iH(t' - t)}{\hbar}\right)|\psi(t)\rangle \quad (3.3)$$

using matrix exponentiation functions. For convenience, \hbar was set to 1 throughout the project. Eq. 3.2 can be derived from Eq. 3.3 by inserting the resolution of the identity $\mathbb{1} = \sum_n |\phi_n\rangle\langle\phi_n|$.

The specific choice of algorithms and their computation times are presented in Appendix B. The propagator method, whose computation time scales favourably as $\mathcal{O}(N)$ with the number of basis states N , was predominantly used; the eigenstate method was occasionally preferable with large values of U or long simulation times.

Occasionally throughout the project, only a partial diagonalization of the Hamiltonian was required; for example, to obtain the eigenspectrum of the doublon band (Section 5.2.1). Here, the Hamiltonian was expressed as a sparse matrix and the Lanczos algorithm [53], which is able to rapidly find a subset of the eigenvalues (though not fully diagonalize the Hamiltonian), was used.

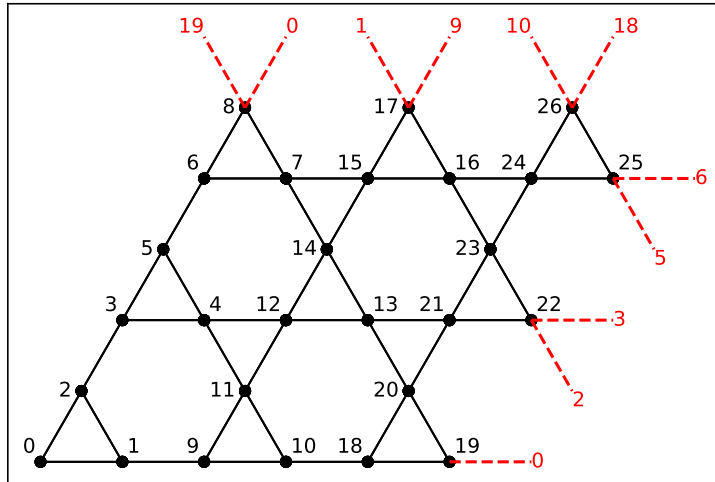


Figure 3.1: Kagome lattice, with sites indexed and periodic boundary conditions illustrated.

4. Single-Particle Simulations

4.1 Single-Site Initial State

The key features of the single-particle behaviour in the kagome lattice are all illustrated by simulations with the particle initially localised to one site, $|\Psi(t=0)\rangle = b_i^\dagger|0\rangle$, as depicted in Fig. 4.1. Since the initial wavefunction is maximally localised in real space, it has equal overlap with all three Bloch bands. As predicted, the density in the dispersive bands spreads throughout the lattice, while the density in the flat band remains localised around the initial site indefinitely.

4.2 Stationary Density

This behaviour can be investigated more quantitatively by calculating the density localised in the vicinity of the original site. This is predicted to tend to $\approx 1/3$, the total density in flat band states. The snapshot of the density in Fig. 4.2(a) shows that most of the stationary density is localised within the two hexagons containing the original site, corresponding to the flat band hexagon states in Fig. 2.2. However, as these states are not a suitable general basis for the flat band, the density in the two hexagons alone is less than $1/3$. The most localised orthonormal basis set for the flat band are the Wannier states, which decay $\sim 1/|\mathbf{r}|$ from their origin [29]. Therefore, to quantify the stationary density, the total density within a small (but arbitrary) radius $r = 1.55a$ of the original site is plotted in Fig. 4.2(b). This tends to 0.33 ± 0.01 , consistent with the theoretical prediction of $1/3$. The fluctuations are due to the dispersive density, which continues to propagate back and forth. This contributes

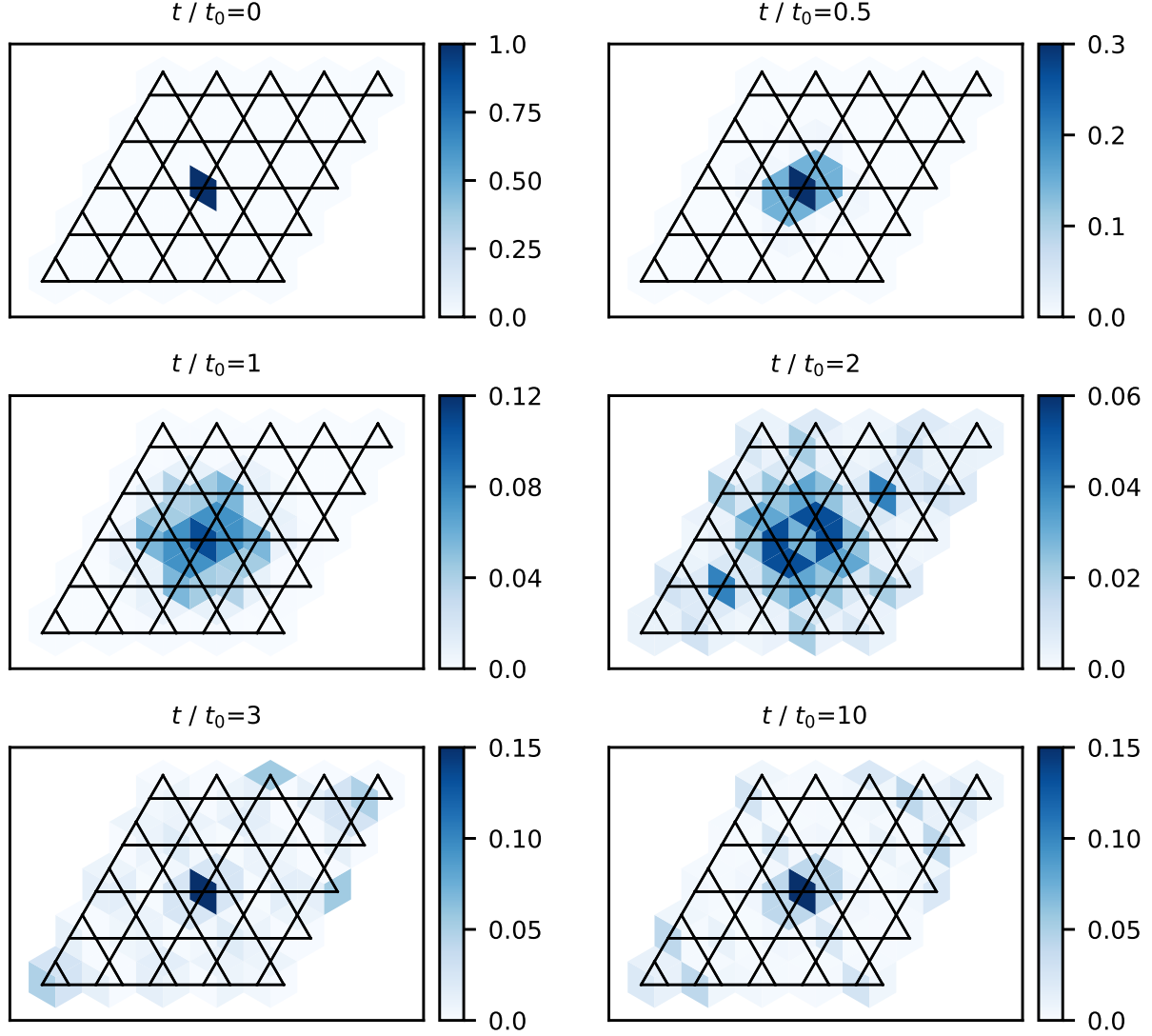


Figure 4.1: Time-evolution of density $\langle n \rangle$ for a single particle initially localised to one site. The small 5×5 unit cell lattice was chosen to enable clear visibility of the expanding density. Note that the colour scale varies between plots. The unit of time is $t_0 = \hbar/J$.

an average density per site of $\approx 2/3$ times the average lattice filling ($1/1200$ for this 20×20 unit cell system), giving a total density of ≈ 0.015 within the $r \leq 1.55a$ region, consistent with the magnitude of the fluctuations.

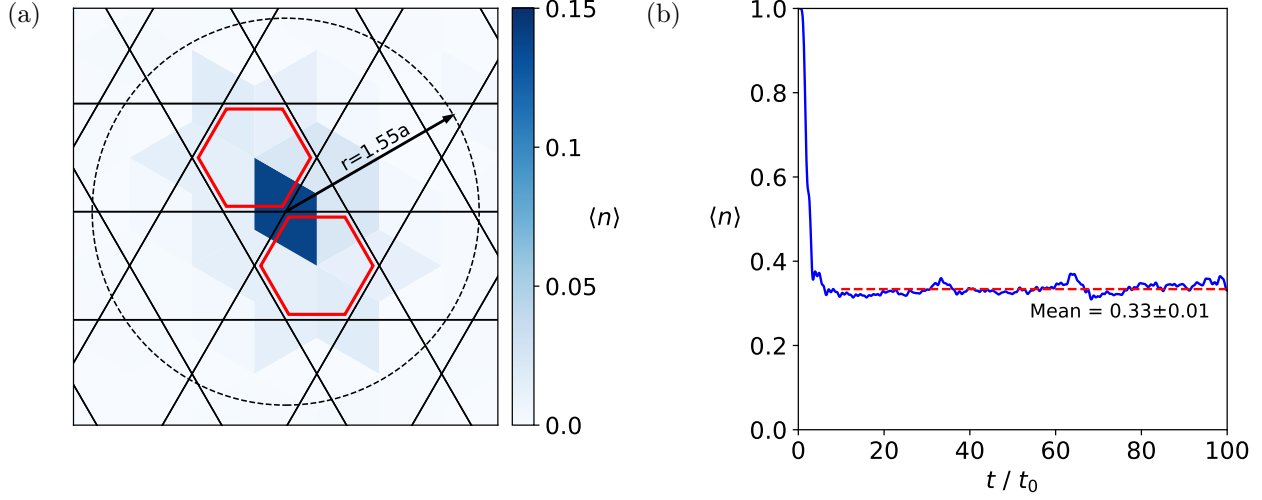


Figure 4.2: Stationary density with a single particle initially localised to one site in a 20×20 unit cell lattice. (a) Snapshot of density at $t = 50t_0$ in the original site vicinity (the full system extends beyond this region). Most density is contained within the two hexagons indicated in red. (b) Time-evolution of total density (blue, solid) within a radius $r = 1.55a$ (indicated in (a)) of the original site. The mean (red, dashed) and standard deviation are calculated for $t \geq 10t_0$. Open boundary conditions were used for this simulation, as the density is susceptible to large fluctuations with periodic boundary conditions.

5. Two-Particle Simulations

5.1 Flat Band Initial State

This section presents two-particle simulations with both particles initially in the same localised flat band hexagon state (as depicted in Fig. 2.2 for a single particle). In terms of the creation operators, this is:

$$|\Psi(t = 0)\rangle = \frac{1}{\sqrt{2}}(h_i^\dagger)^2|0\rangle \quad (5.1a)$$

$$h_i^\dagger = \sum_l \frac{(-1)^l}{\sqrt{6}} b_l^\dagger \quad (5.1b)$$

where l indexes the six sites of hexagon i . Eq. 5.1a will subsequently be referred to as the ‘hexagon initial state’. Since this state is stationary for $U = 0$, the mobility of the particles is solely due to interactions lifting the flat band degeneracy. If the particles were instead initialized on two non-overlapping hexagons, there would be no interaction energy and hence the particles would remain stationary.

Simulations of two interacting particles initially on the same site are presented in Appendix C. These are directly comparable to Section 4; however, the hexagon initial state more effectively illustrates the effect of interactions specifically within the flat band, without the complications of density from the dispersive bands.

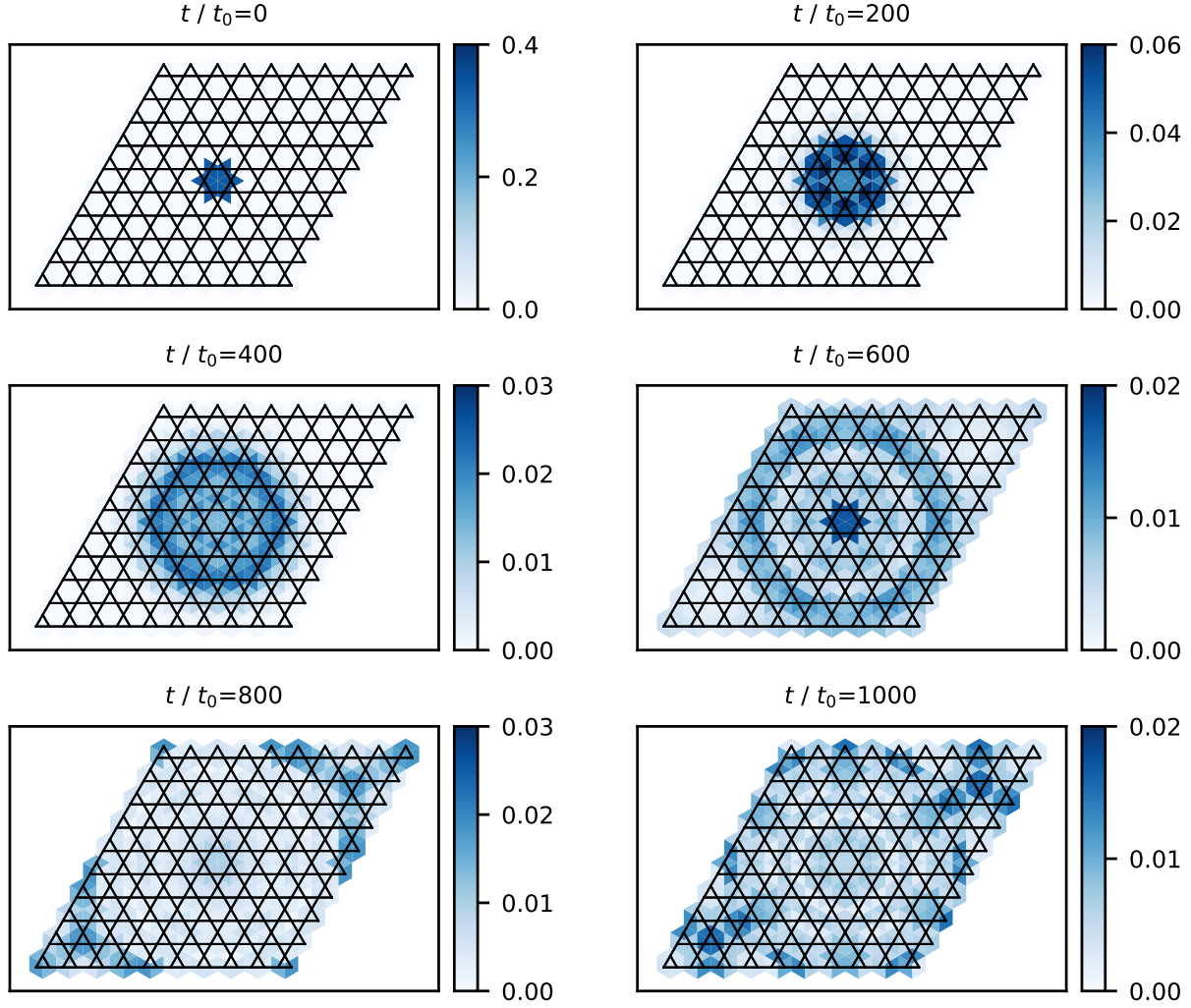


Figure 5.1: Time-evolution of density $\langle n \rangle$ from the hexagon initial state, for $U/J = 0.1$. The lattice size, 10×10 unit cells, is the same throughout Section 5 unless stated otherwise. The colour scale varies between plots.

5.1.1 Dynamical Behaviour and Interaction-Shifted Eigenspectrum

The qualitative behaviour when evolving from the hexagon initial state is illustrated in Fig. 5.1. With $0 < U \ll J$, most of the density spreads symmetrically as a single wavepacket, with little dispersion; a small amount remains stationary in the original hexagon.

This can be explained from the shifts to the energy eigenvalues by the interactions. Fig. 5.2 shows the numerically obtained eigenvalues for pairs of particles, relative to the unperturbed flat band energy, plotted against the magnitude of the total momentum $q = |\mathbf{q}|$ of the eigenstate. The numerical eigenvectors were projected onto the two-particle flat band Bloch states $|\mathbf{k}_1\rangle|\mathbf{k}_2\rangle$ (direct products of Eq. 2.6) to obtain the contributing values of $\mathbf{q} = \mathbf{k}_1 + \mathbf{k}_2$ in each case. As predicted in Section 2.3, the eigenstates are associated with certain \mathbf{q} values. Due to the six-fold rotational symmetry of the kagome lattice, most eigenstates are six-fold degenerate, depending only on the magnitude q not the direction of \mathbf{q} ; Fig. 5.2 does not show this degeneracy explicitly.

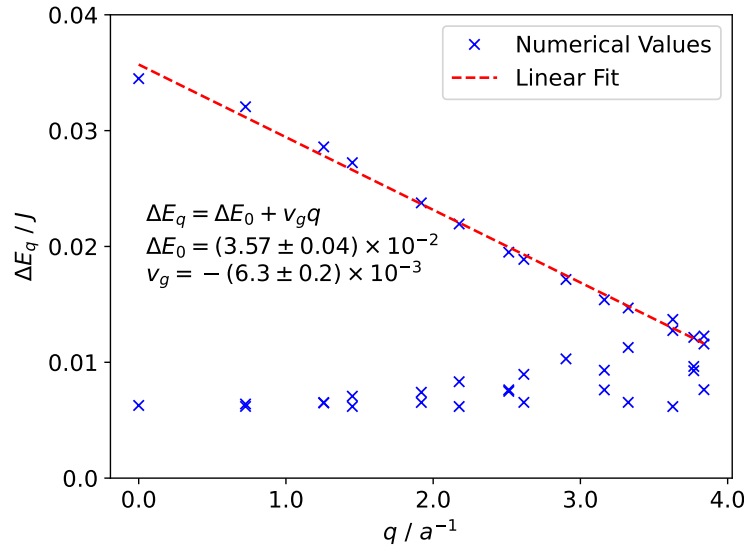


Figure 5.2: Numerically obtained flat band eigenvalues for $U/J = 0.1$, relative to the flat band energy, against the magnitude of the total momentum of the eigenstate. The unperturbed eigenvalues of non-overlapping flat band states are not plotted. A linear fit, giving the group velocity, is performed to the highest-energy eigenvalues at each q .

For the hexagon initial state, $\approx 80\%$ of the density occupies the highest-energy eigenstates whose energy is linear with q in Fig. 5.2. The linear gradient explains the mobile density remaining together as a single wavepacket in Fig. 5.1; all eigenstates have the same group velocity magnitude. Moreover, the isotropic spreading is consistent with ΔE_q depending only on q , not the direction of \mathbf{q} .

The remaining density not occupying these highest-energy states is divided between the lower-energy pair states in Fig. 5.2, unperturbed (non-overlapping) flat band states, and states from the dispersive bands. The lower pair energies are almost dispersionless, which, along with the unperturbed flat band states, explains the stationary and slowly-propagating density visible in the original hexagon and surrounding area at late times in Fig. 5.1. The dispersive states are fast-propagating, and give small fluctuations.

5.1.2 Dependence on Interaction Strength

For systems with larger U , the interaction energy shifts and group velocities are greater. The density in the original hexagon, denoted n_h , therefore decays more quickly, as Fig. 5.3 shows. For $U/J = 0.5$, a peak occurs around $t = 300 t_0$, due to the wavepacket passing completely around the lattice (with its periodic boundary conditions) and recombining in the original hexagon after a certain ‘recombination time’. Fig. 5.3 motivates two methods of quantifying the dependence of the particle mobility on U : the decay time of n_h , and the recombination time (which is inversely proportional to the group velocity). Fig. 5.3 also illustrates that the behaviour becomes more complicated for $U/J \gtrsim 1$. Here, H_U cannot be considered a weak perturbation to H_J , so the hexagon initial state has a mixed character of the flat and dispersive bands. There are therefore components with high group velocities, which rapidly propagate around the lattice, causing the complex fluctuations in n_h .

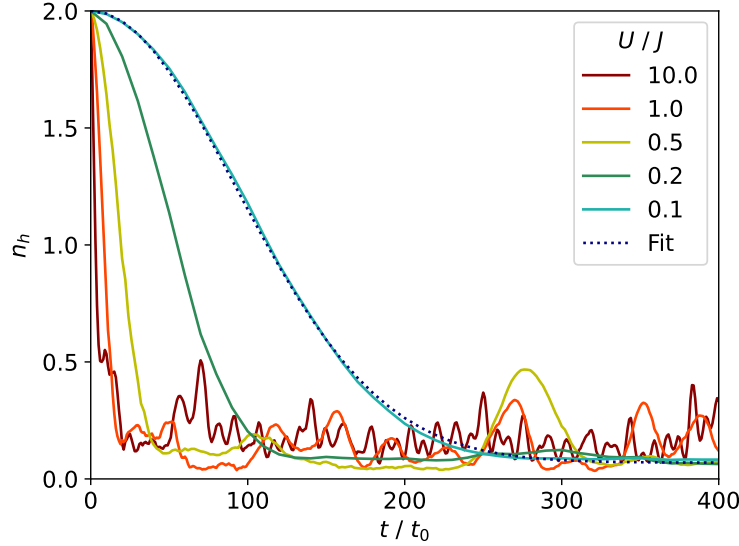


Figure 5.3: Time-evolution of density within the original hexagon, n_h , from simulations with the hexagon initial state, for various interaction strengths. An example curve fitted to the $U/J = 0.1$ data is also plotted (navy, dotted).

For $U/J \lesssim 1$, n_h can be accurately modelled by a Gaussian fitting the initial decay, plus a constant accounting for the stationary density:

$$n_h(t) = (2 - c) \exp\left(-\frac{1}{2} \left(\frac{t}{\tau}\right)^2\right) + c \quad (5.2)$$

The prefactor $2 - c$ ensures $n_h(t = 0) = 2$, consistent with the initial state. Fig. 5.4(a) shows the dependence of the fitted parameter τ on U . For $U \ll J$, fitting a power law gives $\tau \propto U^{-1}$. This is consistent with H_U being a weak perturbation to H_J , causing energy shifts (and therefore particle velocity) $\propto U$ to leading order. The constant c did not vary significantly with U . Fig. 5.4(b) shows the recombination time t_r against U . As with the decay time, $t_r \propto U^{-1}$, implying that $v_g \propto U$. In both plots, higher order effects (deviations from the fitted power laws) are visible beyond $U/J \gtrsim 0.1$.

The group velocity magnitude obtained from the eigenspectrum for $U/J = 0.1$ (Fig. 5.2) is $|v_g| = (6.3 \pm 0.2) \times 10^{-3} a/t_0$ (the sign is unimportant). Using the expression for t_r from Fig. 5.4(b) and the lattice width $L = 10a$ gives the simulation group velocity as $|v_g| = L/t_r = (6.33 \pm 0.05) \times 10^{-3} a/t_0$, demonstrating excellent consistency.

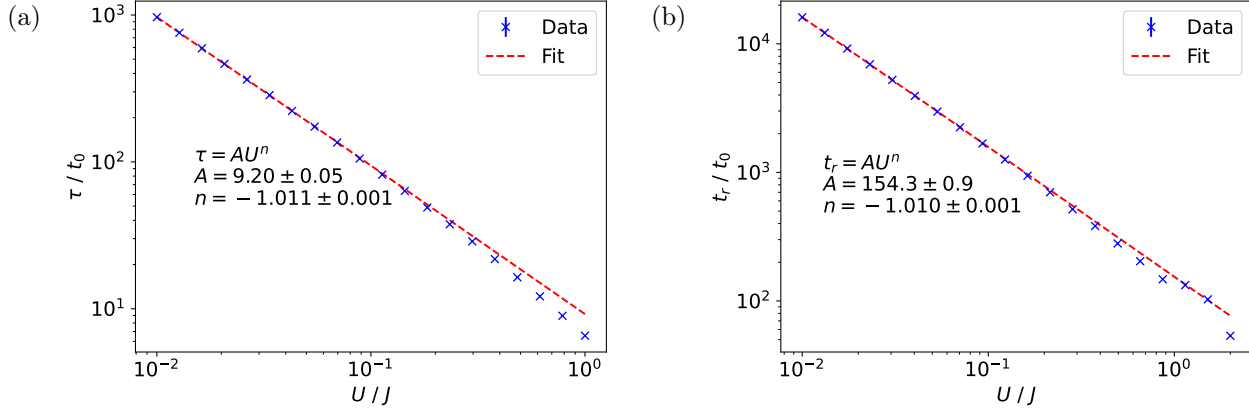


Figure 5.4: (a) Decay time and (b) recombination time of density in the original hexagon, determined from simulations with the hexagon initial state, plotted against interaction strength. Power law fits to the data for $U/J \leq 0.1$ are close to the predicted U^{-1} relationships. The data are only plotted for $U/J \lesssim 1$ where Eq. 5.2 is a good fit to n_h , and t_r is clearly identifiable.

5.1.3 OPDM and Flat Band Projection

The behaviour throughout Section 5.1 has been explained within a weak-perturbation framework: direct products of single-particle flat band states are good two-particle eigenstates, whose mobility is due to interactions lifting their degeneracy, rather than an admixture of states from dispersive bands. This section further verifies this using the one-particle density matrix (OPDM). Following the methodology in [54, 55], the OPDM is defined as:

$$\rho_{ij}(t) = \langle \Psi(t) | b_i^\dagger b_j | \Psi(t) \rangle \quad (5.3)$$

The eigenstates of the OPDM $\{|\phi_\alpha\rangle\}$ are the ‘natural single particle orbitals’ of the system, and the corresponding eigenvalues $\{n_\alpha\}$ their occupancies; $\sum_\alpha n_\alpha = \text{Tr}(\rho) = N$, the number of particles in the system. The total occupancy of single-particle flat band states, N_{FB} , is given by the trace of the OPDM after projecting onto the flat band:

$$N_{\text{FB}} = \text{Tr}(\hat{P}\rho\hat{P}) \quad (5.4a)$$

$$\hat{P} = \sum_{\mathbf{k}} |\mathbf{k}\rangle \langle \mathbf{k}| \quad (5.4b)$$

where $|\mathbf{k}\rangle$ are the single-particle flat band Bloch states (Eq. 2.6).

In general, N_{FB} is not constant in time for states which are not eigenstates of \hat{P} ; therefore, the time-averaged \overline{N}_{FB} is plotted in Fig. 5.5(a). $\overline{N}_{\text{FB}} \approx 2$ and is almost constant for $U/J \ll 1$, confirming that direct products of single-particle flat band states are good two-particle eigenstates. In fact, as Fig. 5.5(b) shows, the ‘non-flat-band occupancy’, $2 - \overline{N}_{\text{FB}}$, is $\propto U^2$ for weak interactions. This is consistent with an admixture of dispersive states within first-order perturbation theory, with amplitude $\propto U$, and therefore occupancy $\propto U^2$.

For $U \gg J$, \overline{N}_{FB} does not decrease all the way to $2/3$ as might be expected from an equal occupancy of all bands. This is because, regardless of the interaction strength, the hexagon initial state is inevitably composed of exact eigenstates which share certain common features with the flat band states, such as alternating signs between sites. Nevertheless, the flat band states are clearly no longer good eigenstates for $U/J \gtrsim 1$, as stated previously when interpreting the system behaviour in this limit.

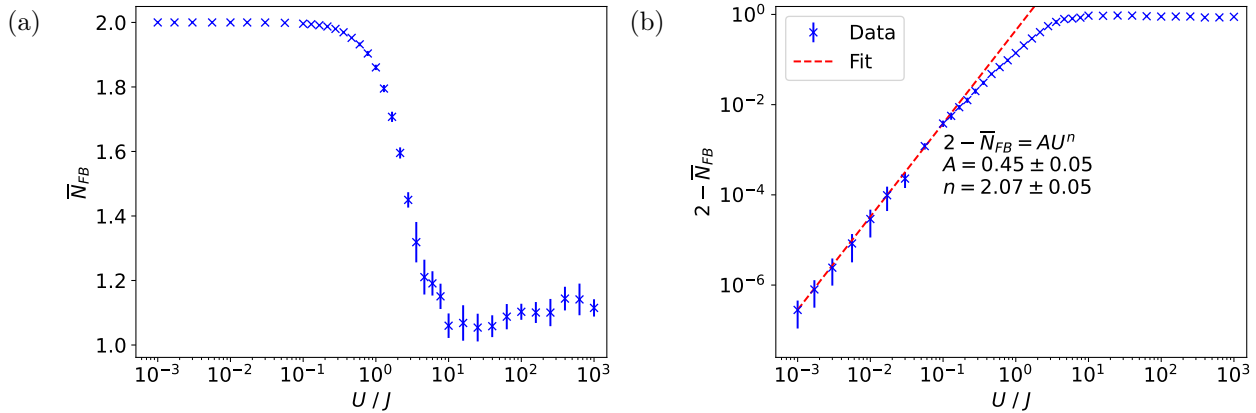


Figure 5.5: Time-averaged (a) flat-band occupancy and (b) non-flat-band occupancy against interaction strength, from simulations with the hexagon initial state. Error bars show the standard deviation of fluctuations. The power law fit in (b) is performed to the data for $U \leq 0.1$.

5.2 Strong Interactions

For strong interactions, $U \gg J$, the eigenspectrum divides into a scattering band and a doublon band, as discussed in Section 2.4. In this section, the theoretical predictions are compared to numerical results, and the resulting dynamical behaviour is examined, for systems with $U/J = 100$.

5.2.1 Eigenspectrum

Fig. 5.6(a) shows the doublon band eigenvalues, which agree closely with those of a single particle with the theoretical effective doublon hopping coefficient from Eq. 2.9. In Appendix D.1, it is verified that discrepancies are due to higher order hopping processes, giving energy shifts $\propto \frac{J^3}{U^2}$.

The scattering band eigenvalues are shown in Fig. 5.6(b) and compared to the non-interacting case. The non-interacting spectrum shows various plateaus of degenerate eigenstates due to the rotational symmetries of the system. With interactions, the degeneracies are partially lifted, for the eigenstates in which the particles overlap in real space. The scattering eigenvalues are virtually unaltered for systems with greater U .

5.2.2 Dynamical Behaviour

For $U \gg J$, doublons cannot separate, and instead propagate through the lattice as a composite particle; this is explicitly verified in Appendix D.2. Fig. 5.7(a) shows the simulation results with two particles initially in a doublon state, $|\Psi(t=0)\rangle = \frac{1}{\sqrt{2}}(b_i^\dagger)^2|0\rangle$. The density in the original site i is plotted against time, and compared to the density simulated for a single particle with the theoretical J_{eff} of the doublon (the constant E_0 does not affect the physical behaviour). The data appear identical up to a re-scaling of the time axis. This is due to the discrepancies between the doublon and effective single-particle eigenspectra in Fig. 5.6(a). These are linear with energy (see Appendix D.1); this linear scaling between the frequency spectra therefore causes the re-scaling of the real-time behaviour.

Fig. 5.7(b) shows the simulation results of two particles initially on different lattice sites,

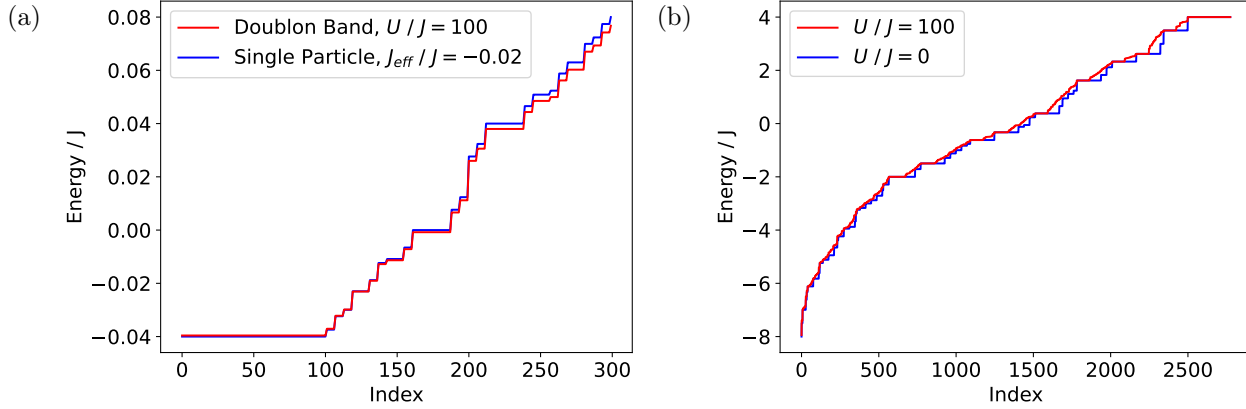


Figure 5.6: Numerically obtained eigenvalues in the strongly-interacting limit, plotted in ascending order (the index is physically meaningless). (a) Doublon band for a 10×10 unit cell system, shifted down by E_0 , compared to single-particle eigenspectrum with $J = J_{\text{eff}}$. E_0 and J_{eff} are defined in Eq. 2.9. (b) Scattering band for 5×5 unit cell systems, for strongly- and non-interacting cases.

$|\Psi(t = 0)\rangle = b_i^\dagger b_j^\dagger |0\rangle$ (a scattering band state). The density in one of the initial sites is plotted against time. For $U/J = 0$, there are large fluctuations due to degenerate eigenstates interfering in phase. With interactions, this degeneracy is partially lifted (see Fig. 5.6(b)), and the fluctuations are less pronounced. This can be intuitively understood as interacting particles repelling each other and spreading uniformly throughout the lattice, instead of propagating together in wavepackets, causing large instantaneous density fluctuations.

5.3 Particle Separation

This section examines the variation of the particle separation during the simulations. This captures several features of the different behaviour regimes discussed above, and the transition between them. For weak interactions, it is verified that particles are only mobile as a bound pair (since spatially-separated states are not shifted in energy); and for strong interactions, the division of doublon and scattering states is further evidenced.

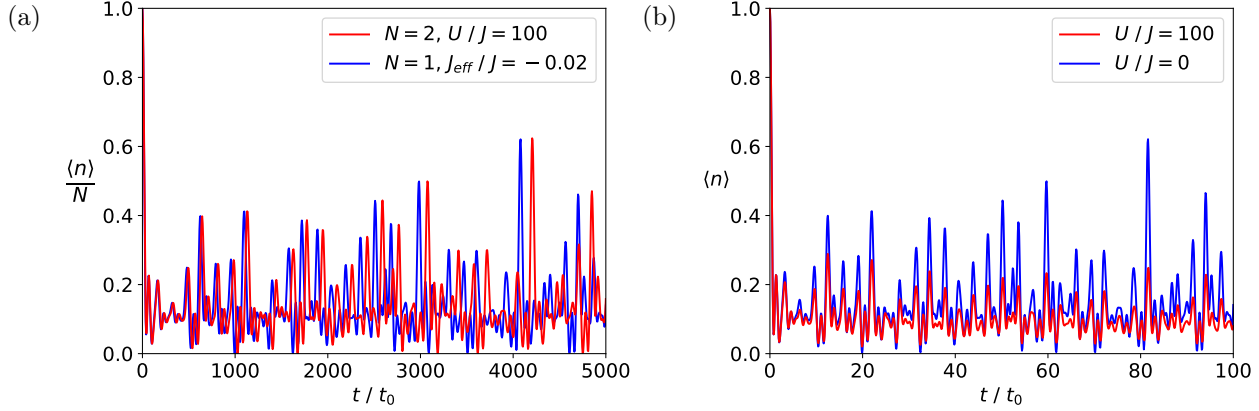


Figure 5.7: Dynamical behaviour of strongly-interacting systems. (a) Time-evolution of density in original site for a single-site initial state, for the strongly-interacting two-particle case, and as calculated using the effective single-particle model Eq. 2.9. The density is normalized by the number of particles, N , to enable comparison of one- and two-particle data. (b) Time-evolution of density in one of the original sites, for particles initially on two different sites, for strongly- and non-interacting cases.

5.3.1 Expected Separation

The expected particle separation is:

$$\langle r \rangle = \sum_{(ij)} |c_{ij}(t)|^2 |\mathbf{r}_i - \mathbf{r}_j| \quad (5.5)$$

where (ij) indicates the exclusion of permutations $ij \rightarrow ji$ to avoid double-counting, $c_{ij}(t) = \langle 0 | b_i b_j | \Psi(t) \rangle$ (with an extra factor of $\frac{1}{\sqrt{2}}$ when $i = j$), and $|\mathbf{r}_i - \mathbf{r}_j|$ is the minimum distance between sites i and j , taking account of the periodic boundary conditions. Fig. 5.8(a) shows $\langle r \rangle$ against time from simulations with the hexagon initial state. For all U , after an initial transient period, $\langle r \rangle$ fluctuates around a steady-state value. The time-averaged steady-state separation $\overline{\langle r \rangle}$ is plotted against U in Fig. 5.8(b). For weak interactions, $\overline{\langle r \rangle} < a$ and is independent of U ; as predicted, the particles are bound closely together, for arbitrarily weak interaction strengths. For $U \gtrsim J$, the two-particle eigenstates are mixtures of the

single-particle flat and dispersive bands, as discussed previously. The particles are therefore independently mobile, so $\overline{\langle r \rangle}$ increases. The large- U value of $\overline{\langle r \rangle}$ is determined only by the lattice geometry, not correlations between the particles; it is on the order of the lattice width ($10a$) divided by 4, due to the periodic boundary conditions.

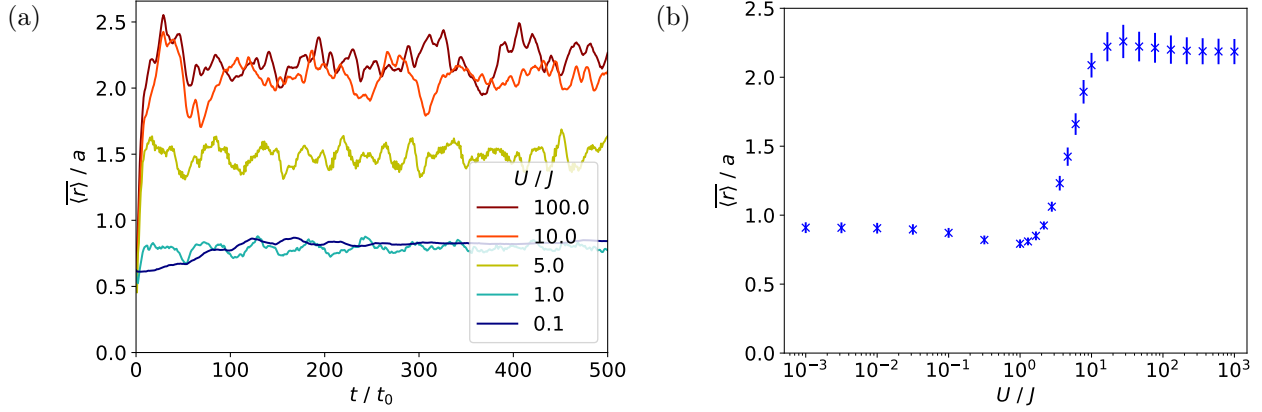


Figure 5.8: (a) Expected particle separation against time from simulations with the hexagon initial state, for various interaction strengths. (b) Time-averaged expected separation (after steady-state has been reached) against interaction strength. Error bars show standard deviations of the fluctuations.

5.3.2 Radial Distribution Function

Additional insight is available from the probability $P(r)$ that the particles occupy any state with sites separated by r :

$$P(r) = \sum_{(ij)} |c_{ij}|^2 \delta_{r, |\mathbf{r}_i - \mathbf{r}_j|} \quad (5.6)$$

where $\delta_{r, |\mathbf{r}_i - \mathbf{r}_j|}$ is the Kronecker delta; only discrete values of r determined by the lattice are possible. The expected separation $\langle r \rangle$ is equal to $\sum_r r P(r)$. In fact, a more convenient quantity to interpret is the ‘radial distribution function’ $g(r)$, defined as $P(r)$ divided by the

number of basis states consisting of sites separated by r , $N(r)$:

$$g(r) = \frac{P(r)}{N(r)} = \frac{\sum_{(ij)} |c_{ij}|^2 \delta_{r, |\mathbf{r}_i - \mathbf{r}_j|}}{\sum_{(ij)} \delta_{r, |\mathbf{r}_i - \mathbf{r}_j|}} \quad (5.7)$$

With no correlations between particles, all basis states have an equal chance of being occupied; $g(r)$ is therefore constant, and equal to $1/N_{\text{states}}$.

For different initial states and interaction strengths, $g(r)$ was calculated at each evolution timestep. As with $\langle r \rangle$, $g(r)$ tends to a steady-state distribution after an initial transient period. Fig. 5.9 shows the time-averaged steady-state $g(r)$. With the particles initially on different sites (Fig. 5.9(a)), a peak remains around $r = 2a$. This is due to the stationary flat band density localised around each of the original sites, as in the single-particle simulations of Section 4. Since the two sites are separated, the flat band eigenstates localised around each site do not overlap one another, and therefore have no interaction energy shift and remain stationary. For other values of r and weak interactions, $g(r)$ is close to the constant value expected with no correlations between particles. For strong interactions, $g(r)$ is similar to the weak-interaction case for most values of r , except $g(r = 0) \approx 0$; doublon states are inaccessible for this initial scattering state, as expected.

For the hexagon initial state (Fig. 5.9(b)), for weak interactions $g(r)$ is largest around $r = 0$, and decreases to almost 0 for $r \gtrsim a$. This supports Section 5.3.1 in confirming that the particles are bound together as they move. For strong interactions, there is a peak at $r = 0$ due to the initial occupancy of doublon states which are subsequently unable to separate. $g(r > 0)$ is almost uniform, showing the absence of correlations between the particles away from $r = 0$ in the scattering band.

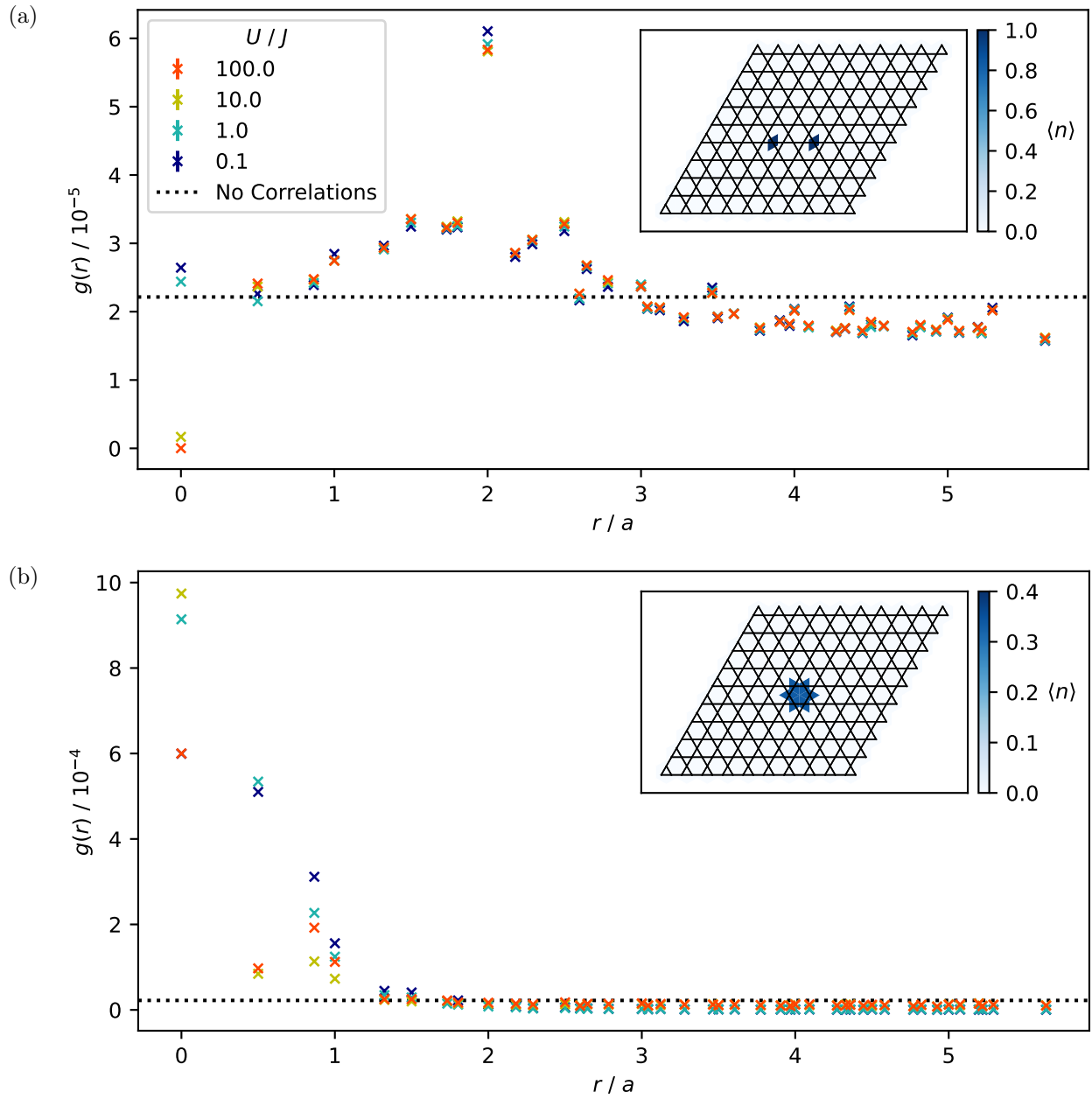


Figure 5.9: Time-averaged steady-state radial distribution functions for (a) particles initially on separate sites, and (b) the hexagon initial state. Insets show the initial density distributions. The legend in (a) applies to both plots. Error bars indicating the standard deviation of fluctuations in $g(r)$ are too small to be seen for most points.

6. Conclusions

This report has presented the results of computational simulations of one and two bosons in a kagome lattice. The single-particle behaviour can be fully understood from the bandstructure of the system. Particles in the dispersive bands of the system are mobile, whereas particles in the flat band are stationary and remain localised in the vicinity of their initial position.

Two-particle systems have been studied across the full range of interaction strengths. For weak interactions, direct products of single particle Bloch states are good two-particle eigenstates, but with eigenvalues shifted by the interaction energy. This lifts the flat band degeneracy, enabling the transport of bound pairs of particles. Particles in spatially separated flat band states have zero interaction energy, and hence remain stationary.

With strong interactions, the system eigenspectrum divides into a doublon band and scattering band. States in the two bands cannot inter-convert due to the prohibitively large interaction energy cost. Systems composed of scattering states behave qualitatively similarly to systems of non-interacting particles, with the difference that the density tends to distribute more evenly throughout the lattice. The doublon behaviour is well-described by an effective single-particle Hamiltonian; the particles are bound together on the same site as they propagate.

This project has highlighted the rich physics that arises from interactions between just two particles in a flat band. It is natural to ask whether systems with more particles can be understood through the microscopic behaviour elucidated in this report, or whether larger, collective descriptions are required. To investigate this question, with greater computing power, similar exact simulations for slightly greater numbers of particles could be performed. Beyond this, approximations, such as mean-field methods, would be required. Accordingly, it

is plausible that experiments, in particular with cold atoms, are able to make greater progress in the exploration of flat band systems than numerical research.

Beyond higher particle numbers, other extensions to this work could include considering the effect of the external trapping potential used in cold atom experiments, and a greater variety of initial states. The results presented throughout this report provide a broad, solid foundation on which to develop understanding for these additional cases.

A. Pair Energy in Isolated Flat Band Limit

This appendix presents the expressions derived in [46] for the interaction energy shift to a pair of particles in the flat band. By assuming that the flat band is isolated from the other bands by an energy gap $\gg U$, the two-particle eigenstates can justifiably be expanded only in terms of the single-particle flat band Bloch states. As there is no external potential with a different periodicity to the lattice, the total momentum of the particles, $\mathbf{q} = \mathbf{k}_1 + \mathbf{k}_2$, is conserved, and is therefore a good quantum number which can be used to label the eigenstates. The energy shifts relative to the flat band, $\Delta E_{\mathbf{q}}$, are found to satisfy the eigenvalue equation:

$$\sum_{\mathbf{k}'} V_{\mathbf{k}\mathbf{k}'}(\mathbf{q}) A_{\mathbf{k}'} = \Delta E_{\mathbf{q}} A_{\mathbf{k}} \quad (\text{A.1a})$$

$$V_{\mathbf{k}\mathbf{k}'}(\mathbf{q}) = \frac{U}{N_c} \sum_{\alpha} m_{\mathbf{k}',\alpha}^* m_{\mathbf{q}-\mathbf{k}',\alpha}^* m_{\mathbf{k},\alpha} m_{\mathbf{q}-\mathbf{k},\alpha} \quad (\text{A.1b})$$

with $m_{\mathbf{k},\alpha}$ the flat band eigenvector components defined in Eq. 2.5 (the label ⁽³⁾ is omitted). Most eigenvalues of $V_{\mathbf{k}\mathbf{k}'}$ are zero, corresponding to the unperturbed non-overlapping flat band states. $V_{\mathbf{k}\mathbf{k}'}$ can be approximated by:

$$V_{\mathbf{k}\mathbf{k}'}(\mathbf{q}) \approx V'_{\mathbf{k}\mathbf{k}'}(\mathbf{q}) = \frac{U}{N_c} \frac{1}{N_{\text{orb}}} (\mathbf{m}_{\mathbf{k}'}^* \cdot \mathbf{m}_{\mathbf{q}-\mathbf{k}'}^*) (\mathbf{m}_{\mathbf{k}} \cdot \mathbf{m}_{\mathbf{q}-\mathbf{k}}) \quad (\text{A.2})$$

where N_{orb} is the number of orbitals in each unit cell ($N_{\text{orb}} = 3$ for the kagome lattice). This enables the eigenvalue equation A.1 to be solved to give:

$$\Delta E_{\mathbf{q}} = \frac{U}{N_c} \frac{1}{N_{\text{orb}}} \sum_{\mathbf{k}} |\mathbf{m}_{\mathbf{k}} \cdot \mathbf{m}_{\mathbf{q}-\mathbf{k}}|^2 \quad (\text{A.3})$$

Since this expression is the trace of the approximated interaction matrix $V'_{\mathbf{k}\mathbf{k}'}$, all other eigenvalues of $V'_{\mathbf{k}\mathbf{k}'}$ are zero.

Fig. A.1 below compares (i) the numerically obtained eigenvalues of the full Hamiltonian (as in Fig. 5.2), (ii) the numerically obtained eigenvalues of $V_{\mathbf{k}\mathbf{k}'}$, and (iii) the energies calculated using Eq. A.3, for a 10×10 unit cell system and $U/J = 0.1$. Since the isolated flat band condition is not satisfied for the kagome lattice, there is some admixture of dispersive states in the exact case (i); however, the resultant errors in the case (ii) values are minor. Case (iii) involves the additional approximation of $V_{\mathbf{k}\mathbf{k}'}$ by $V'_{\mathbf{k}\mathbf{k}'}$, and only gives a single energy value for each q ; despite this, these values agree extremely closely with the largest eigenvalues of $V_{\mathbf{k}\mathbf{k}'}$.

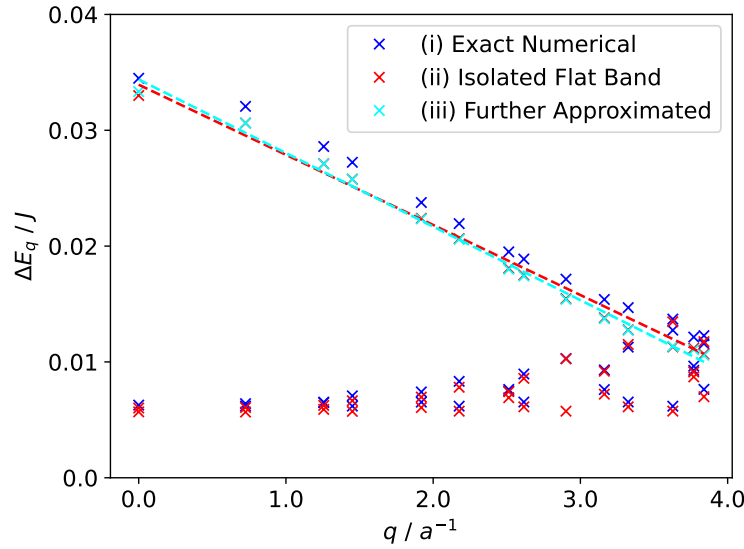


Figure A.1: Energy shifts of bound particle pairs relative to the flat band energy level, for $U/J = 0.1$ in a 10×10 unit cell system, plotted against magnitude of total momentum q . Numerical eigenvalues from diagonalizing the full Hamiltonian are shown in dark blue; eigenvalues of the interaction matrices $V_{\mathbf{k}\mathbf{k}'}(\mathbf{q})$ (Eq. A.1) in red; energies calculated from Eq. A.3 in light blue. Note that these light blue points are almost coincident with the highest of the red points at each q . Linear fits to the highest energy values at each q are shown dashed in the respective colours of the datasets.

For both case (ii) and (iii), the highest-energy eigenvalues have approximately the same gradient as the exact spectrum, and therefore can be used to accurately estimate the group velocity. Linear fits to the data were performed to obtain the respective group velocities, (ii) $v_g = (6.1 \pm 0.2) \times 10^{-3} a/t_0$ and (iii) $v_g = (6.4 \pm 0.1) \times 10^{-3} a/t_0$. These closely match the values obtained previously in Section 5.1.2: $v_g = (6.3 \pm 0.2) \times 10^{-3} a/t_0$ from the exact eigenspectrum, and $v_g = (6.33 \pm 0.05) \times 10^{-3} a/t_0$ from the simulation. In fact, the value from the case (iii) turns out to be more accurate despite the additional approximations involved.

In practice, the expressions throughout this appendix are of limited use for performing dynamical simulations, as in this project. As Appendix B will describe, calculating observables from the state $|\Psi\rangle$, not the time-evolution to find $|\Psi(t)\rangle$, is frequently the computationally limiting step of the simulations. Hence, these approximate expressions may enable faster calculation of the energies and time-evolution, but do not significantly improve the computational capabilities. Instead, they are useful for evaluating quantities which depend only on the eigenspectrum. These include the group velocity, as illustrated above, and the effective mass of the bound particle pairs, as is done in [46].

B. Further Computational Details

B.1 Comparison of Numerical Routines

Full diagonalization of the Hamiltonian H was performed using the `eigh` function in NumPy and SciPy. A comparison of the in-built diagonalization routines (Fig. B.1) found that the `evd` driver performed the best, with diagonalization time following the formula:

$$t_{\text{diag}} \approx N^3 \times 1.2 \times 10^{-10} \text{ s} \quad (\text{B.1})$$

Throughout this appendix, N refers to the number of basis states, not the number of particles. For the two-particle, 10×10 unit cell system considered throughout much of this project, $N \approx 4.5 \times 10^4$. As well as the diagonalization of H , the eigenstate evolution method (Eq. 3.2) also requires a summation of $\mathcal{O}(N^2)$ terms per timestep, with computation time found to be:

$$t_{\text{eig}} \approx N^2 \times 1.1 \times 10^{-8} \text{ s} \quad (\text{B.2})$$

Evolution in the propagator method (Eq. 3.3) was calculated by expressing the Hamiltonian as a sparse matrix, and using the SciPy function `expm_multiply`; this far out-performed calculating the exponential using `expm`, and then separately multiplying it with the state vector. For $J = \hbar = 1$, the time for this operation was found to be:

$$t_{\text{prop}} \approx NU\Delta t \times 1.0 \times 10^{-6} \text{ s} \quad (\text{B.3})$$

where Δt is the evolution time. The propagator method nearly always performed the best, both due to avoiding the $\mathcal{O}(N^3)$ full diagonalization of the Hamiltonian, and because the cost per timestep is only $\mathcal{O}(N)$, not $\mathcal{O}(N^2)$. In fact, the limiting step with the propagator

method was often found to be the $\mathcal{O}(N)$ calculation of observables (such as the density $\langle n \rangle$) from the state $|\Psi\rangle$, not the time-evolution. As the eigenstate method is independent of Δt and U , it was nevertheless occasionally preferable for certain simulations. Furthermore, the diagonalization only needs to be performed once; thereafter, the eigenvalues and eigenvectors can be used to compute the time-evolution of various initial states.

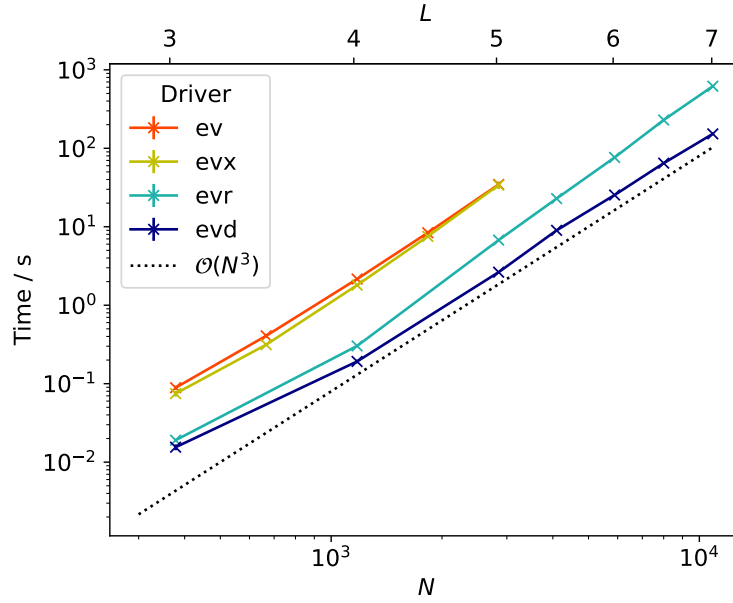


Figure B.1: Comparison of computation time for diagonalization of the Hamiltonian matrix, of dimension $N \times N$, for different driver routines. The values of L for which a 2-particle, $L \times L$ unit cell system has N basis states are shown on the upper x -axis. The dotted line is a guide to the eye, not the fitted relationship for t_{diag} . Error bars from the random error in repeating the computations are too small to be visible.

B.2 Three-Particle Computation Time

To leading order, N scales as $N_{\text{sites}}^{N_A}/N_A!$, where N_A is the number of particles in the system. With the limited computing power and time available for the project, this highly unfavourable scaling with N_A prevented any investigation of systems with $N_A > 2$. As a concrete example, for the two-particle system with 10×10 unit cells generally investigated throughout the project, collecting a small dataset such as the one used in Fig. 5.7(b) takes ≈ 4 minutes, with calculating the density the limiting step. Performing an equivalent simulation for a three-particle system would take over six hours; other simulations could be expected to take several days. Performing meaningful research, involving running multiple simulations, was therefore infeasible within the timeframe for the project. Simulations could instead be performed on much smaller systems; 5×5 unit cells would give a similar number of basis states with three particles as 10×10 unit cells with two particles. However, the results of such simulations would likely be severely affected by finite size effects.

C. Single-Site Initial State with Interactions

This appendix contains the results of simulations of two interacting particles, with $U = J$, initially on the same site. This gives a direct comparison to the single-particle simulations in Section 4; however, since all Bloch bands are occupied, the behaviour is more complicated to analyse than the simulations which were instead presented in Section 5.1 with the hexagon initial state.

Fig. C.1 shows the density within $r = 1.55 a$ of the original site against time, as in Fig. 4.2. With $U \neq 0$, the particles do not remain localised indefinitely; instead, the density decays to ~ 0.1 (approximately the value expected due to the average lattice filling). This qualitatively shows the effect of the interactions: the flat band degeneracy is lifted, and so the particles become mobile.

The particle velocity in the flat band is significantly lower than in the dispersive bands, demonstrated by the timescales for the density in the original site vicinity to decay in Fig. C.1 (~ 100 s of t_0) and Fig. 4.2 ($\sim 10 t_0$). This is why simulations with this initial state are challenging to analyse more quantitatively. The dispersive density rapidly propagates around the lattice and interferes with the flat band density which is still slowly propagating away from the initial site, making it difficult to reliably extract parameters such as the decay time of the flat band density.

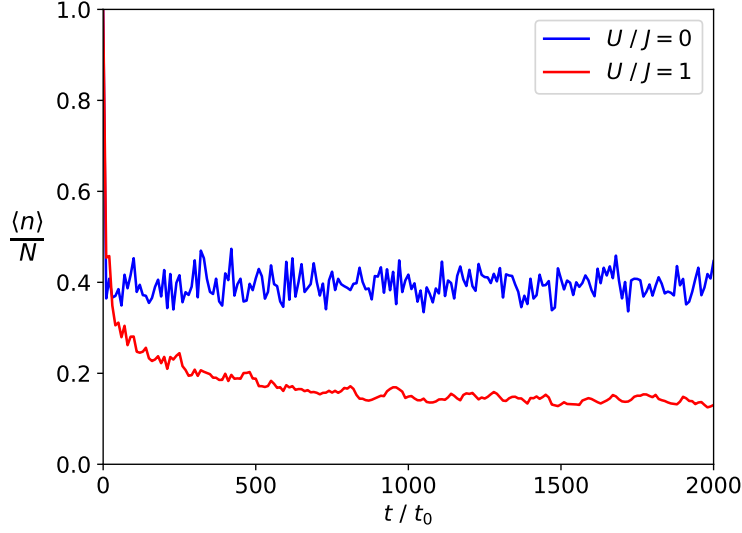


Figure C.1: Simulations of two particles initially on the same site, for interacting and non-interacting cases. Density within $r = 1.55a$ of the initial site is plotted against time, as in Fig. 4.2. The density is normalized by the number of particles, $N = 2$, to facilitate comparison to Fig. 4.2. The average lattice filling is higher for this 10×10 unit cell lattice than for the 20×20 lattice simulated in Section 4.2, hence the density with $U/J = 0$ remains significantly above $1/3$. Open boundary conditions were used for these simulations, as in Section 4.2.

D. Further Strong-Interaction Results

D.1 Higher-Order Corrections to Doublon Energies

This appendix presents details of the higher-order corrections to the effective doublon Hamiltonian. Fig. D.1(a) shows the difference ΔE between the the effective single-particle energies calculated using Eq. 2.9, and numerical doublon energies, E_d (with the energy offset E_0 subtracted). ΔE is found to scale linearly with E_d . This explains the observed dynamical behaviour in Fig. 5.7(a), where the data for the doublons and the effective single particle appear identical up to a linear re-scaling of the time axis.

Fig. D.1(b) demonstrates that ΔE arises due to next-highest-order hopping processes, giving energy corrections $\propto \frac{J^3}{U^2}$. The plot shows that the fitted linear gradient of ΔE with E_d is $\propto U^{-1}$. Since the gradient is $\propto \frac{\Delta E}{E_d}$, and $E_d \propto U^{-1}$ to leading order, this demonstrates that $\Delta E \propto U^{-2}$, as predicted.

This scaling of ΔE with U does not explain why the relationship between ΔE and E_d should be linear. Since the values involved are $\ll 1$, it is possible that this linear behaviour is the leading order term of a more complicated relationship. Alternatively, there may be an underlying theoretical reason that the relationship is truly linear; the extremely high accuracy of the linear fit seems to support this. As this is only a minor detail in understanding the doublon behaviour, it was not investigated further.

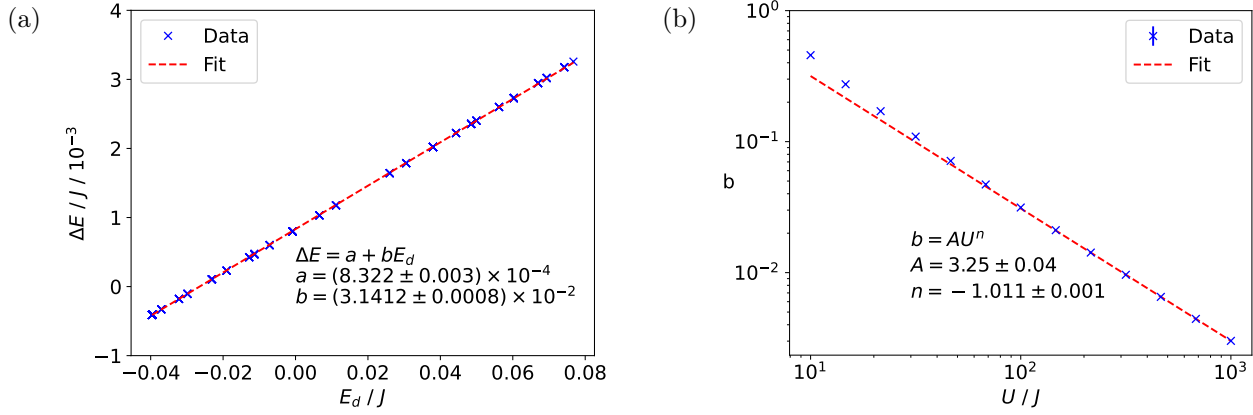


Figure D.1: (a) Energy difference ΔE between numerical doublon energies, E_d , and effective single-particle energies (Eq. 2.9), against E_d , for $U/J = 100$. The energy offset E_0 is subtracted from E_d . A linear fit is performed to the data. (b) Values of the gradient, b , fitted to data of ΔE against E_d (as depicted in (a)), for different U . The power law fit is performed to the data for $U \geq 100$.

D.2 Doublon Fraction

In this appendix, it is verified that for $U \gg J$, particles initially in a doublon state do not separate, but instead remain together as a composite particle. The doublon fraction, or probability that the two particles occupy a doublon state, at time t is:

$$P_d(t) = \sum_i |\langle d_i | \Psi(t) \rangle|^2 \quad (\text{D.1})$$

The sum runs over lattice sites i . Fig. D.2(a) shows $P_d(t)$ for simulations with two particles initially in a doublon state (on the same site), for various U . In all cases, there is an initial transient period, before a steady-state period of fluctuations around a constant mean value. The time-averaged steady-state $\overline{P_d}$ is plotted against U in Fig. D.2(b). For $U/J \gg 1$, this tends to 1; as expected, the particles cannot separate, and instead the doublon propagates through the lattice as a composite particle. Furthermore, in Fig. D.2(c), $1 - \overline{P_d}$ decreases $\propto U^{-2}$ for large U . This is consistent with a perturbation-theory admixture of scattering

states, with amplitude $\propto U^{-1}$ and therefore probability $\propto U^{-2}$. For weak interactions, $\overline{P}_d \sim N_{\text{sites}}/N_{\text{states}}$, the value expected for no correlations; the particles equally occupy all N_{states} basis states, of which N_{sites} are doublon states. This value is slightly exceeded due to the large spikes in P_d visible in Fig. D.2(a), which are due to degenerate eigenstates interfering in phase. As with the simulation of scattering states in Fig. 5.7(b), stronger interactions lift this degeneracy, suppressing the spikes.

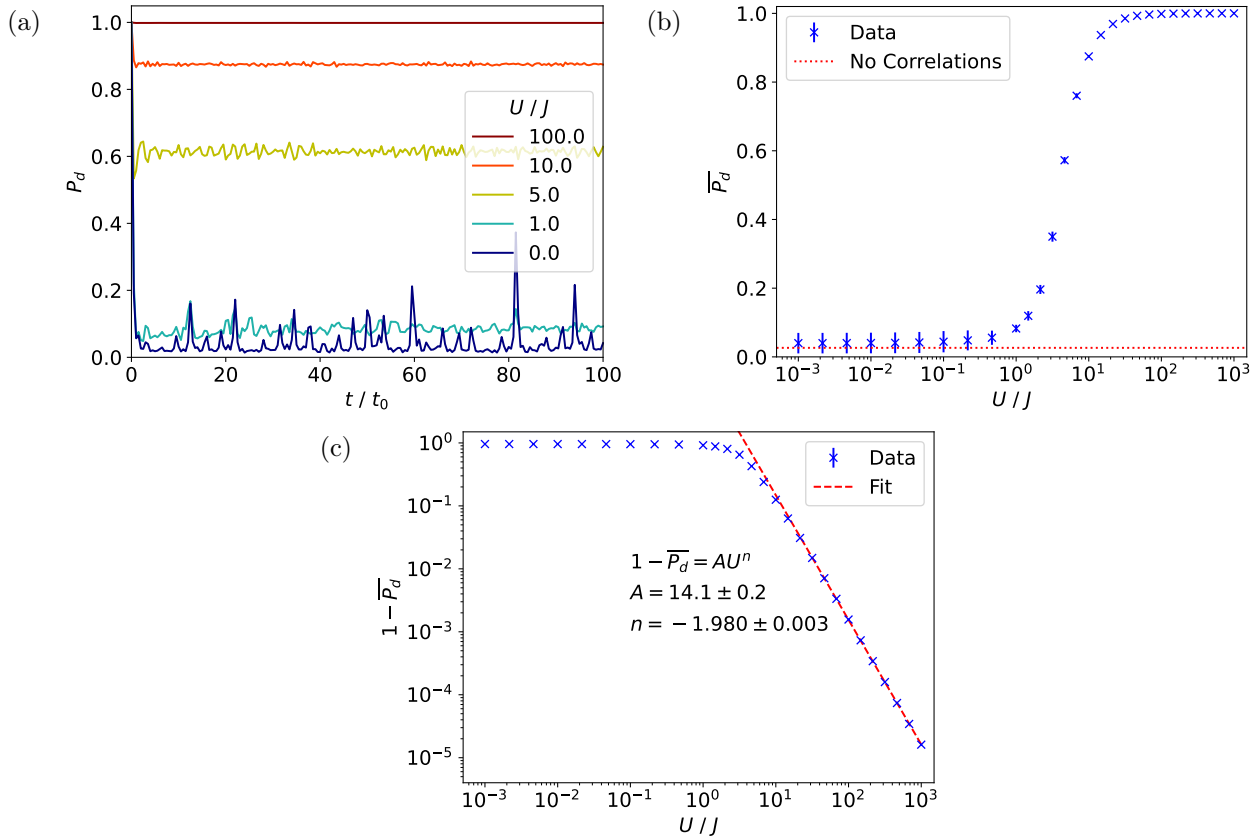


Figure D.2: (a) Doublon probability against time for simulations with an initial doublon state, for various interaction strengths. (b) Doublon probability, averaged for $t \geq 10t_0$, against interaction strength. Error bars show standard deviations of the fluctuations. Red dotted line shows the value expected for no correlations, $N_{\text{sites}}/N_{\text{states}}$. (c) Time-averaged non-doublon probability against interaction strength, with log scale. The power law fit is performed to the data with $U \geq 30$.

Bibliography

- [1] Alexei Andreanov Daniel Leykam and Sergej Flach. “Artificial flat band systems: from lattice models to experiments”. In: *Advances in Physics: X* 3.1 (2018), p. 1473052. DOI: [10.1080/23746149.2018.1473052](https://doi.org/10.1080/23746149.2018.1473052).
- [2] Titus Neupert et al. “Fractional Quantum Hall States at Zero Magnetic Field”. In: *Phys. Rev. Lett.* 106 (23 June 2011), p. 236804. DOI: [10.1103/PhysRevLett.106.236804](https://doi.org/10.1103/PhysRevLett.106.236804). URL: <https://link.aps.org/doi/10.1103/PhysRevLett.106.236804>.
- [3] Evelyn Tang, Jia-Wei Mei, and Xiao-Gang Wen. “High-Temperature Fractional Quantum Hall States”. In: *Phys. Rev. Lett.* 106 (23 June 2011), p. 236802. DOI: [10.1103/PhysRevLett.106.236802](https://doi.org/10.1103/PhysRevLett.106.236802). URL: <https://link.aps.org/doi/10.1103/PhysRevLett.106.236802>.
- [4] Siddharth A. Parameswaran, Rahul Roy, and Shivaji L. Sondhi. “Fractional quantum Hall physics in topological flat bands”. In: *Comptes Rendus Physique* 14.9 (2013). Topological insulators / Isolants topologiques, pp. 816–839. ISSN: 1631-0705. DOI: <https://doi.org/10.1016/j.crhy.2013.04.003>. URL: <https://www.sciencedirect.com/science/article/pii/S163107051300073X>.
- [5] Julian Léonard et al. “Realization of a fractional quantum Hall state with ultracold atoms”. In: *Nature* 619.7970 (July 2023), pp. 495–499. ISSN: 1476-4687. DOI: [10.1038/s41586-023-06122-4](https://doi.org/10.1038/s41586-023-06122-4). URL: <https://doi.org/10.1038/s41586-023-06122-4>.
- [6] T Kida et al. “The giant anomalous Hall effect in the ferromagnet Fe₃Sn₂—a frustrated kagome metal”. In: *Journal of Physics: Condensed Matter* 23.11 (Mar. 2011), p. 112205.

- ISSN: 1361-648X. DOI: [10.1088/0953-8984/23/11/112205](https://doi.org/10.1088/0953-8984/23/11/112205). URL: <http://dx.doi.org/10.1088/0953-8984/23/11/112205>.
- [7] Enke Liu et al. “Giant anomalous Hall effect in a ferromagnetic kagome-lattice semimetal”. In: *Nature Physics* 14.11 (Nov. 2018), pp. 1125–1131. ISSN: 1745-2481. DOI: [10.1038/s41567-018-0234-5](https://doi.org/10.1038/s41567-018-0234-5). URL: <https://doi.org/10.1038/s41567-018-0234-5>.
- [8] Stephan Rachel. “Interacting topological insulators: a review”. In: *Reports on Progress in Physics* 81.11 (Oct. 2018), p. 116501. DOI: [10.1088/1361-6633/aad6a6](https://doi.org/10.1088/1361-6633/aad6a6). URL: <https://dx.doi.org/10.1088/1361-6633/aad6a6>.
- [9] Kai Sun et al. “Nearly Flatbands with Nontrivial Topology”. In: *Phys. Rev. Lett.* 106 (23 June 2011), p. 236803. DOI: [10.1103/PhysRevLett.106.236803](https://link.aps.org/doi/10.1103/PhysRevLett.106.236803). URL: <https://link.aps.org/doi/10.1103/PhysRevLett.106.236803>.
- [10] Doron L. Bergman, Congjun Wu, and Leon Balents. “Band touching from real-space topology in frustrated hopping models”. In: *Phys. Rev. B* 78 (12 Sept. 2008), p. 125104. DOI: [10.1103/PhysRevB.78.125104](https://link.aps.org/doi/10.1103/PhysRevB.78.125104). URL: <https://link.aps.org/doi/10.1103/PhysRevB.78.125104>.
- [11] Jia-Xin Yin, Biao Lian, and M. Zahid Hasan. “Topological kagome magnets and superconductors”. In: *Nature* 612.7941 (Dec. 2022), pp. 647–657. ISSN: 1476-4687. DOI: [10.1038/s41586-022-05516-0](https://doi.org/10.1038/s41586-022-05516-0). URL: <https://doi.org/10.1038/s41586-022-05516-0>.
- [12] Zhi Li et al. “Realization of flat band with possible nontrivial topology in electronic Kagome lattice”. In: *Science Advances* 4.11 (2018), eaau4511. DOI: [10.1126/sciadv.aau4511](https://doi.org/10.1126/sciadv.aau4511). eprint: <https://www.science.org/doi/pdf/10.1126/sciadv.aau4511>. URL: <https://www.science.org/doi/abs/10.1126/sciadv.aau4511>.
- [13] Mingu Kang et al. “Topological flat bands in frustrated kagome lattice CoSn”. In: *Nature Communications* 11.1 (Aug. 2020), p. 4004. ISSN: 2041-1723. DOI: [10.1038/s41467-020-17465-1](https://doi.org/10.1038/s41467-020-17465-1). URL: <https://doi.org/10.1038/s41467-020-17465-1>.

- [14] N. B. Kopnin, T. T. Heikkilä, and G. E. Volovik. “High-temperature surface superconductivity in topological flat-band systems”. In: *Phys. Rev. B* 83 (22 June 2011), p. 220503. DOI: [10.1103/PhysRevB.83.220503](https://doi.org/10.1103/PhysRevB.83.220503). URL: <https://link.aps.org/doi/10.1103/PhysRevB.83.220503>.
- [15] Masatoshi Sato and Yoichi Ando. “Topological superconductors: a review”. In: *Reports on Progress in Physics* 80.7 (May 2017), p. 076501. DOI: [10.1088/1361-6633/aa6ac7](https://doi.org/10.1088/1361-6633/aa6ac7). URL: <https://dx.doi.org/10.1088/1361-6633/aa6ac7>.
- [16] Cenke Xu and Leon Balents. “Topological Superconductivity in Twisted Multilayer Graphene”. In: *Phys. Rev. Lett.* 121 (8 Aug. 2018), p. 087001. DOI: [10.1103/PhysRevLett.121.087001](https://doi.org/10.1103/PhysRevLett.121.087001). URL: <https://link.aps.org/doi/10.1103/PhysRevLett.121.087001>.
- [17] Matthew Yankowitz et al. “Tuning superconductivity in twisted bilayer graphene”. In: *Science* 363.6431 (2019), pp. 1059–1064. DOI: [10.1126/science.aav1910](https://doi.org/10.1126/science.aav1910). eprint: <https://www.science.org/doi/pdf/10.1126/science.aav1910>. URL: <https://www.science.org/doi/abs/10.1126/science.aav1910>.
- [18] C Mielke III et al. “Local spectroscopic evidence for a nodeless magnetic kagome superconductor CeRu₂”. In: *Journal of Physics: Condensed Matter* 34.48 (Oct. 2022), p. 485601. DOI: [10.1088/1361-648X/ac9813](https://doi.org/10.1088/1361-648X/ac9813). URL: <https://dx.doi.org/10.1088/1361-648X/ac9813>.
- [19] Z. Guguchia, R. Khasanov, and H. Luetkens. “Unconventional charge order and superconductivity in kagome-lattice systems as seen by muon-spin rotation”. In: *npj Quantum Materials* 8.1 (Aug. 2023), p. 41. ISSN: 2397-4648. DOI: [10.1038/s41535-023-00574-7](https://doi.org/10.1038/s41535-023-00574-7). URL: <https://doi.org/10.1038/s41535-023-00574-7>.
- [20] S. V. Isakov et al. “Hard-Core Bosons on the Kagome Lattice: Valence-Bond Solids and Their Quantum Melting”. In: *Phys. Rev. Lett.* 97 (14 Oct. 2006), p. 147202. DOI: [10.1103/PhysRevLett.97.147202](https://doi.org/10.1103/PhysRevLett.97.147202). URL: <https://link.aps.org/doi/10.1103/PhysRevLett.97.147202>.

- [21] Yi-Zhuang You et al. “Superfluidity of Bosons in Kagome Lattices with Frustration”. In: *Phys. Rev. Lett.* 109 (26 Dec. 2012), p. 265302. DOI: [10.1103/PhysRevLett.109.265302](https://doi.org/10.1103/PhysRevLett.109.265302). URL: <https://link.aps.org/doi/10.1103/PhysRevLett.109.265302>.
- [22] Hosho Katsura et al. “Mott-insulator-like Bose-Einstein condensation in a tight-binding system of interacting bosons with a flat band”. In: *Phys. Rev. Res.* 3 (3 Aug. 2021), p. 033190. DOI: [10.1103/PhysRevResearch.3.033190](https://doi.org/10.1103/PhysRevResearch.3.033190). URL: <https://link.aps.org/doi/10.1103/PhysRevResearch.3.033190>.
- [23] Bill Sutherland. “Localization of electronic wave functions due to local topology”. In: *Phys. Rev. B* 34 (8 Oct. 1986), pp. 5208–5211. DOI: [10.1103/PhysRevB.34.5208](https://doi.org/10.1103/PhysRevB.34.5208). URL: <https://link.aps.org/doi/10.1103/PhysRevB.34.5208>.
- [24] Elliott H. Lieb. “Two theorems on the Hubbard model”. In: *Phys. Rev. Lett.* 62 (10 Mar. 1989), pp. 1201–1204. DOI: [10.1103/PhysRevLett.62.1201](https://doi.org/10.1103/PhysRevLett.62.1201). URL: <https://link.aps.org/doi/10.1103/PhysRevLett.62.1201>.
- [25] Itiro Syôzi. “Statistics of Kagomé Lattice”. In: *Progress of Theoretical Physics* 6.3 (June 1951). _eprint: <https://academic.oup.com/ptp/article-pdf/6/3/306/5239621/6-3-306.pdf>, pp. 306–308. ISSN: 0033-068X. DOI: [10.1143/ptp/6.3.306](https://doi.org/10.1143/ptp/6.3.306). URL: <https://doi.org/10.1143/ptp/6.3.306>.
- [26] Sergei V. Isakov, Arun Paramekanti, and Yong Baek Kim. “Exotic phase diagram of a cluster charging model of bosons on the kagome lattice”. In: *Phys. Rev. B* 76 (22 Dec. 2007), p. 224431. DOI: [10.1103/PhysRevB.76.224431](https://doi.org/10.1103/PhysRevB.76.224431). URL: <https://link.aps.org/doi/10.1103/PhysRevB.76.224431>.
- [27] H.-M. Guo and M. Franz. “Topological insulator on the kagome lattice”. In: *Phys. Rev. B* 80 (11 Sept. 2009), p. 113102. DOI: [10.1103/PhysRevB.80.113102](https://doi.org/10.1103/PhysRevB.80.113102). URL: <https://link.aps.org/doi/10.1103/PhysRevB.80.113102>.
- [28] Krishanu Roychowdhury, Subhro Bhattacharjee, and Frank Pollmann. “ \mathbb{Z}_2 topological liquid of hard-core bosons on a kagome lattice at 1/3 filling”. In: *Phys. Rev. B* 92 (7 Aug. 2015), p. 075141. DOI: [10.1103/PhysRevB.92.075141](https://doi.org/10.1103/PhysRevB.92.075141). URL: <https://link.aps.org/doi/10.1103/PhysRevB.92.075141>.

- [29] Sebastian D. Huber and Ehud Altman. “Bose condensation in flat bands”. In: *Phys. Rev. B* 82 (18 Nov. 2010), p. 184502. DOI: [10.1103/PhysRevB.82.184502](https://doi.org/10.1103/PhysRevB.82.184502). URL: <https://link.aps.org/doi/10.1103/PhysRevB.82.184502>.
- [30] Aleksi Julku, Georg M. Bruun, and Päivi Törmä. “Quantum Geometry and Flat Band Bose-Einstein Condensation”. In: *Phys. Rev. Lett.* 127 (17 Oct. 2021), p. 170404. DOI: [10.1103/PhysRevLett.127.170404](https://doi.org/10.1103/PhysRevLett.127.170404). URL: <https://link.aps.org/doi/10.1103/PhysRevLett.127.170404>.
- [31] Aleksi Julku, Georg M. Bruun, and Päivi Törmä. “Excitations of a Bose-Einstein condensate and the quantum geometry of a flat band”. In: *Phys. Rev. B* 104 (14 Oct. 2021), p. 144507. DOI: [10.1103/PhysRevB.104.144507](https://doi.org/10.1103/PhysRevB.104.144507). URL: <https://link.aps.org/doi/10.1103/PhysRevB.104.144507>.
- [32] David A. Huse and Andrew D. Rutenberg. “Classical antiferromagnets on the Kagomé lattice”. In: *Phys. Rev. B* 45 (13 Apr. 1992), pp. 7536–7539. DOI: [10.1103/PhysRevB.45.7536](https://doi.org/10.1103/PhysRevB.45.7536). URL: <https://link.aps.org/doi/10.1103/PhysRevB.45.7536>.
- [33] L. Balents, M. P. A. Fisher, and S. M. Girvin. “Fractionalization in an easy-axis Kagome antiferromagnet”. In: *Phys. Rev. B* 65 (22 May 2002), p. 224412. DOI: [10.1103/PhysRevB.65.224412](https://doi.org/10.1103/PhysRevB.65.224412). URL: <https://link.aps.org/doi/10.1103/PhysRevB.65.224412>.
- [34] X. Plat et al. “Magnetization plateaus of an easy-axis kagome antiferromagnet with extended interactions”. In: *Phys. Rev. B* 92 (17 Nov. 2015), p. 174402. DOI: [10.1103/PhysRevB.92.174402](https://doi.org/10.1103/PhysRevB.92.174402). URL: <https://link.aps.org/doi/10.1103/PhysRevB.92.174402>.
- [35] C. Broholm et al. “Quantum spin liquids”. In: *Science* 367.6475 (2020), eaay0668. DOI: [10.1126/science.aay0668](https://doi.org/10.1126/science.aay0668). eprint: <https://www.science.org/doi/pdf/10.1126/science.aay0668>. URL: <https://www.science.org/doi/abs/10.1126/science.aay0668>.

- [36] Immanuel Bloch, Jean Dalibard, and Wilhelm Zwerger. “Many-body physics with ultracold gases”. In: *Rev. Mod. Phys.* 80 (3 July 2008), pp. 885–964. DOI: [10.1103/RevModPhys.80.885](https://doi.org/10.1103/RevModPhys.80.885). URL: <https://link.aps.org/doi/10.1103/RevModPhys.80.885>.
- [37] Christian Gross and Immanuel Bloch. “Quantum simulations with ultracold atoms in optical lattices”. In: *Science* 357.6355 (2017), pp. 995–1001. DOI: [10.1126/science.aal3837](https://doi.org/10.1126/science.aal3837). eprint: <https://www.science.org/doi/pdf/10.1126/science.aal3837>. URL: <https://www.science.org/doi/abs/10.1126/science.aal3837>.
- [38] Tim Langen, Remi Geiger, and Jörg Schmiedmayer. “Ultracold Atoms Out of Equilibrium”. In: *Annual Review of Condensed Matter Physics* 6.1 (2015), pp. 201–217. DOI: [10.1146/annurev-conmatphys-031214-014548](https://doi.org/10.1146/annurev-conmatphys-031214-014548). eprint: <https://doi.org/10.1146/annurev-conmatphys-031214-014548>. URL: <https://doi.org/10.1146/annurev-conmatphys-031214-014548>.
- [39] Anatoli Polkovnikov et al. “Colloquium: Nonequilibrium dynamics of closed interacting quantum systems”. In: *Rev. Mod. Phys.* 83 (3 Aug. 2011), pp. 863–883. DOI: [10.1103/RevModPhys.83.863](https://doi.org/10.1103/RevModPhys.83.863). URL: <https://link.aps.org/doi/10.1103/RevModPhys.83.863>.
- [40] Gyu-Boong Jo et al. “Ultracold Atoms in a Tunable Optical Kagome Lattice”. In: *Phys. Rev. Lett.* 108 (4 Jan. 2012), p. 045305. DOI: [10.1103/PhysRevLett.108.045305](https://doi.org/10.1103/PhysRevLett.108.045305). URL: <https://link.aps.org/doi/10.1103/PhysRevLett.108.045305>.
- [41] S. Braun et al. “Negative Absolute Temperature for Motional Degrees of Freedom”. In: *Science* 339.6115 (2013), pp. 52–55. DOI: [10.1126/science.1227831](https://doi.org/10.1126/science.1227831). eprint: <https://www.science.org/doi/pdf/10.1126/science.1227831>. URL: <https://www.science.org/doi/abs/10.1126/science.1227831>.
- [42] D. Jaksch and P. Zoller. “The cold atom Hubbard toolbox”. In: *Annals of Physics* 315.1 (2005). Special Issue, pp. 52–79. ISSN: 0003-4916. DOI: <https://doi.org/10.1016/j.aop.2004.09.010>. URL: <https://www.sciencedirect.com/science/article/pii/S0003491604001782>.

- [43] Gia-Wei Chern, Chih-Chun Chien, and Massimiliano Di Ventra. “Dynamically generated flat-band phases in optical kagome lattices”. In: *Phys. Rev. A* 90 (1 July 2014), p. 013609. DOI: [10.1103/PhysRevA.90.013609](https://doi.org/10.1103/PhysRevA.90.013609). URL: <https://link.aps.org/doi/10.1103/PhysRevA.90.013609>.
- [44] V. Apaja, M. Hyrkäs, and M. Manninen. “Flat bands, Dirac cones, and atom dynamics in an optical lattice”. In: *Phys. Rev. A* 82 (4 Oct. 2010), p. 041402. DOI: [10.1103/PhysRevA.82.041402](https://doi.org/10.1103/PhysRevA.82.041402). URL: <https://link.aps.org/doi/10.1103/PhysRevA.82.041402>.
- [45] M. Hyrkäs, V. Apaja, and M. Manninen. “Many-particle dynamics of bosons and fermions in quasi-one-dimensional flat-band lattices”. In: *Phys. Rev. A* 87 (2 Feb. 2013), p. 023614. DOI: [10.1103/PhysRevA.87.023614](https://doi.org/10.1103/PhysRevA.87.023614). URL: <https://link.aps.org/doi/10.1103/PhysRevA.87.023614>.
- [46] P. Törmä, L. Liang, and S. Peotta. “Quantum metric and effective mass of a two-body bound state in a flat band”. In: *Phys. Rev. B* 98 (22 Dec. 2018), p. 220511. DOI: [10.1103/PhysRevB.98.220511](https://doi.org/10.1103/PhysRevB.98.220511). URL: <https://link.aps.org/doi/10.1103/PhysRevB.98.220511>.
- [47] Hideki Ozawa et al. “Interaction-Driven Shift and Distortion of a Flat Band in an Optical Lieb Lattice”. In: *Phys. Rev. Lett.* 118 (17 Apr. 2017), p. 175301. DOI: [10.1103/PhysRevLett.118.175301](https://doi.org/10.1103/PhysRevLett.118.175301). URL: <https://link.aps.org/doi/10.1103/PhysRevLett.118.175301>.
- [48] Tsz-Him Leung et al. “Interaction-Enhanced Group Velocity of Bosons in the Flat Band of an Optical Kagome Lattice”. In: *Phys. Rev. Lett.* 125 (13 Sept. 2020), p. 133001. DOI: [10.1103/PhysRevLett.125.133001](https://doi.org/10.1103/PhysRevLett.125.133001). URL: <https://link.aps.org/doi/10.1103/PhysRevLett.125.133001>.
- [49] M Valiente and D Petrosyan. “Two-particle states in the Hubbard model”. In: *Journal of Physics B: Atomic, Molecular and Optical Physics* 41.16 (Aug. 2008), p. 161002. DOI: [10.1088/0953-4075/41/16/161002](https://doi.org/10.1088/0953-4075/41/16/161002). URL: <https://dx.doi.org/10.1088/0953-4075/41/16/161002>.

- [50] Andreas Deuchert et al. “Dynamics and symmetries of a repulsively bound atom pair in an infinite optical lattice”. In: *Phys. Rev. A* 86 (1 July 2012), p. 013618. DOI: [10.1103/PhysRevA.86.013618](https://doi.org/10.1103/PhysRevA.86.013618). URL: <https://link.aps.org/doi/10.1103/PhysRevA.86.013618>.
- [51] K. Winkler et al. “Repulsively bound atom pairs in an optical lattice”. In: *Nature* 441.7095 (June 2006), pp. 853–856. ISSN: 1476-4687. DOI: [10.1038/nature04918](https://doi.org/10.1038/nature04918). URL: <https://doi.org/10.1038/nature04918>.
- [52] G. Salerno et al. “Interaction-induced lattices for bound states: Designing flat bands, quantized pumps, and higher-order topological insulators for doublons”. In: *Phys. Rev. Res.* 2 (1 Mar. 2020), p. 013348. DOI: [10.1103/PhysRevResearch.2.013348](https://doi.org/10.1103/PhysRevResearch.2.013348). URL: <https://link.aps.org/doi/10.1103/PhysRevResearch.2.013348>.
- [53] Alexander Weiße and Holger Fehske. “Exact diagonalization techniques”. In: *Computational many-particle physics* (2008), pp. 529–544.
- [54] Soumya Bera et al. “Many-Body Localization Characterized from a One-Particle Perspective”. In: *Phys. Rev. Lett.* 115 (4 July 2015), p. 046603. DOI: [10.1103/PhysRevLett.115.046603](https://doi.org/10.1103/PhysRevLett.115.046603). URL: <https://link.aps.org/doi/10.1103/PhysRevLett.115.046603>.
- [55] Talía L. M. Lezama et al. “One-particle density matrix occupation spectrum of many-body localized states after a global quench”. In: *Phys. Rev. B* 96 (6 Aug. 2017), p. 060202. DOI: [10.1103/PhysRevB.96.060202](https://doi.org/10.1103/PhysRevB.96.060202). URL: <https://link.aps.org/doi/10.1103/PhysRevB.96.060202>.